

Article

Control of osteoblast regeneration by a train of Erk activity waves

<https://doi.org/10.1038/s41586-020-03085-8>

Received: 8 October 2019

Accepted: 19 November 2020

Published online: 6 January 2021

 Check for updates

Alessandro De Simone^{1,2}, Maya N. Evanitsky^{1,2}, Luke Hayden^{1,2}, Ben D. Cox^{1,2,6}, Julia Wang^{1,2}, Valerie A. Tornini^{1,2,7}, Jianhong Ou¹, Anna Chao^{1,2}, Kenneth D. Poss^{1,2,3,4} & Stefano Di Talia^{1,2,5}

Regeneration is a complex chain of events that restores a tissue to its original size and shape. The tissue-wide coordination of cellular dynamics that is needed for proper morphogenesis is challenged by the large dimensions of regenerating body parts. Feedback mechanisms in biochemical pathways can provide effective communication across great distances^{1–5}, but how they might regulate growth during tissue regeneration is unresolved^{6,7}. Here we report that rhythmic travelling waves of Erk activity control the growth of bone in time and space in regenerating zebrafish scales, millimetre-sized discs of protective body armour. We find that waves of Erk activity travel across the osteoblast population as expanding concentric rings that are broadcast from a central source, inducing ring-like patterns of tissue growth. Using a combination of theoretical and experimental analyses, we show that Erk activity propagates as excitable trigger waves that are able to traverse the entire scale in approximately two days and that the frequency of wave generation controls the rate of scale regeneration. Furthermore, the periodic induction of synchronous, tissue-wide activation of Erk in place of travelling waves impairs tissue growth, which indicates that wave-distributed Erk activation is key to regeneration. Our findings reveal trigger waves as a regulatory strategy to coordinate cell behaviour and instruct tissue form during regeneration.

The ultimate size and shape of a tissue are determined by the patterns of growth and division of its cellular constituents. The challenges of visualizing dynamic cell behaviours and signalling pathways in real time have limited the ability to investigate mechanisms of regeneration in adult animals. Here, we apply transgenic tools, live imaging, quantitative analysis and mathematical modelling to investigate how signalling dynamics regulate bone regeneration in adult zebrafish.

Zebrafish scales are disc-shaped dermal bones that are arranged in an array to form a skeletal armour^{8–13} (Fig. 1a, Extended data Fig. 1a). As in mammalian dermal bones, the mineral matrix of the scale is directly deposited by adjacent osteoblasts¹⁴. Scale osteoblasts include two populations: a monolayer of large ‘central osteoblasts’ and a peripheral rim of smaller ‘marginal osteoblasts’¹¹ (Fig. 1b, Extended Data Fig. 1b). Each scale sits in a dermal pocket and is covered by epidermis^{8–13} (Fig. 1a). Scales that are dislodged and shed upon physical contact with another fish or object can regenerate within two weeks^{8–11} (Extended Data Fig. 1a). Following scale loss, a pool of new osteoblasts is established within two days by de novo differentiation¹⁰. For a brief period, scale growth proceeds by proliferation of this founder osteoblast pool¹⁰ (Fig. 1b–d; unless noted otherwise, osteoblasts are visualized using a nuclear osx:H2A–mCherry marker¹⁰ (*osx* is also known as *sp7*)). After this (by around four days after plucking), scales reach their final number of central osteoblasts, which continue to grow via cellular hypertrophy^{10,11} (Fig. 1b–d, Extended Data Fig. 1c). 5-ethynyl-2'-deoxyuridine

(EdU)-incorporation labelling indicated that central osteoblasts do not undergo DNA replication during scale hypertrophy (Extended Data Fig. 1d). Furthermore, we marked central osteoblasts during the hypertrophic phase using the photoconvertible protein mEos2 fused to a histone protein and traced them during the following days, finding no evidence that they were proliferative, apoptotic or migratory (Extended Data Fig. 1e–h).

To investigate the spatial organization of osteoblast growth, we tracked osteoblast positions over 6- to 12-h periods, reconstructed tissue movements and used vector calculus to generate maps of tissue expansion and contraction (Methods). The expansion of the osteoblast tissue within each regenerating scale was not uniform, but occurred in disc- or ring-like patterns (Fig. 1e, Extended Data Fig. 1i).

To examine a possible signalling basis for these patterns of tissue expansion, we generated a transgenic line that enables live visualization of a proxy for the activity of Erk kinase (Erk kinase translocation reporter (KTR)¹⁵) (Fig. 2a, b), which was implicated by inhibition experiments (Extended Data Fig. 2a). The Erk KTR sensor provides a readout of the spatiotemporal activation of Erk signalling through measurement of its relative cytoplasmic and nuclear levels, as the sub-cellular localization of the sensor is controlled by Erk phosphorylation (Fig. 2a). Thus, the sensor accumulates in the nucleus at low levels of Erk activity and shuttles to the cytoplasm at high levels of Erk activity (Fig. 2a). By visualizing the biosensor together with a nuclear marker

¹Regeneration Next, Duke University, Durham, NC, USA. ²Department of Cell Biology, Duke University Medical Center, Durham, NC, USA. ³Department of Biology, Duke University, Durham, NC, USA. ⁴Department of Medicine, Duke University Medical Center, Durham, NC, USA. ⁵Department of Orthopaedic Surgery, Duke University Medical Center, Durham, NC, USA. ⁶Present address: Department of Molecular and Cellular Biology, University of California, Davis, Davis, CA, USA. ⁷Present address: Department of Genetics, Yale University School of Medicine, New Haven, CT, USA. [✉]e-mail: kenneth.poss@duke.edu; stefano.ditalia@duke.edu

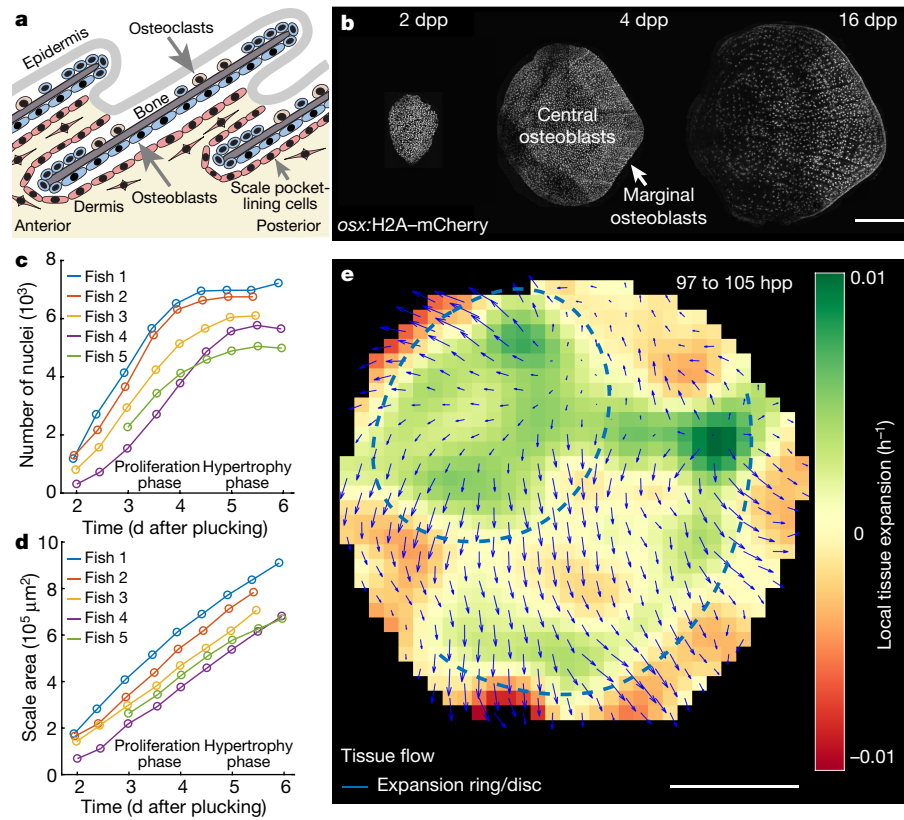


Fig. 1 | Scale regeneration proceeds by patterned hypertrophy of osteoblasts. **a, b**, Zebrafish scale morphology and regeneration. $n > 50$ fish from > 5 independent experiments. **c, d**, Number of nuclei and scale area during regeneration. Data are from a single trial, replicated in 1 additional independent experiment. **e**, Tissue velocity field \bar{v} (tissue flow, blue arrows)

and its divergence $\nabla \cdot \bar{v}$ (heat map), indicating tissue expansion and contraction. $n > 10$ fish from 5 independent experiments. Dashed line, ring of tissue expansion; red, high tissue contraction; green, high tissue expansion. Scale bars, 250 μm . dpp, days post-plucking; hpp, hours post-plucking.

and applying automated image processing, we could ratiometrically quantify Erk activity in the population of scale osteoblasts at any given time (Fig. 2b, c, Methods).

Erk is regulated by many ligand-receptor tyrosine kinase partners, of which fibroblast growth factors (Fgf) and their receptors are candidates in scales^{8,10}. We performed several pharmacological and transgenic perturbations, which indicated that Erk activity in scale osteoblasts depends on Fgf receptors and the activation of MAPKK (Fig. 3a, Extended Data Figs. 2b–d, 3, 4, 5j, Supplementary Notes). Erk activity decreased rapidly (in around 3 h) after Fgf receptor blockade (Extended Data Fig. 3c), but not after inhibition of epidermal growth factor (Egf) receptors (Extended Data Fig. 3h, i, Methods). Furthermore, ectopic expression of an Fgf ligand was sufficient to ectopically activate Erk signalling in scales (Extended Data Fig. 4c–f).

To assess Erk signalling in regenerating osteoblasts, we imaged scales at several time points after plucking. Erk activity was high throughout the osteoblast pool from 1 until 2–3 days after injury (Extended Data Fig. 2e), then diminished starting near the centre of the scale before the onset of the hypertrophic phase at around 3 days after plucking. After this point, high levels of Erk activity localized in ring-shaped regions (Fig. 2b, c) that varied in size and localization between scales and fish (Figs. 2c, 4a, Extended Data Figs. 2–8). Thus, osteoblast Erk signalling activates in a similar spatial pattern to that of tissue expansion during scale regeneration.

To identify whether Erk activity rings might be dynamic, we monitored Erk signalling longitudinally in individual regenerating scales over several days. Notably, we found that rings of high levels of Erk activity travel across the tissue as a wave, moving from one cell to the other. In particular, multiple high Erk-activity rings expand from a

source region located between the centre and the anterior margin of the scale and move towards its periphery (Fig. 2c, d, Supplementary Video 1). Erk waves travel at a speed about 10 $\mu\text{m h}^{-1}$: one wave therefore traverses the entire scale in about 2 days (Fig. 2c–e). Near the completion of this journey, a new wave emerges at the same source (Fig. 2c). By tracking individual cells, we observed Erk oscillations with an activation time of around 3 h and inactivation time of around 5 h (Fig. 2f) that established a travelling front that was 50–100 μm wide (Fig. 2c, d). Monitoring the entire period of regeneration longitudinally (over about 2 weeks), we observed 5 or 6 Erk waves in each scale (Fig. 2g, Supplementary Video 2). Thus, our findings indicate that Erk signalling is activated in a series of repeated, concentric waves that travel across the osteoblast population.

We next considered how Erk activity is organized in travelling waves. Diffusible signals can generate excitable ‘trigger waves’ in reaction–diffusion systems that include positive and negative feedback^{5,16} (Fig. 3a). For example, if a diffusible signal—for example, an Fgf ligand—activates Erk and if cells in which Erk is active stimulate and/or produce a diffusible activator, this would generate a spreading activity wave. However, as Erk signalling travels as a localized peak (Fig. 2d–f), a mechanism of delayed inactivation is required, potentially adjudicated by the Erk-responsive dual-specificity phosphatases (Dusp) and Sprouty proteins¹⁷. To identify the presence of potential Erk inhibitory factors during wave propagation, we developed a strategy to compare the transcriptomes of sorted osteoblasts that display either elevated or reduced Erk activity (Extended Data Fig. 5a–g, Supplementary Notes). These experiments indicated that the expression levels of *dusp5* and *spry4* are elevated in osteoblasts in which Erk is active (Extended Data Fig. 5h–j, Supplementary Notes).

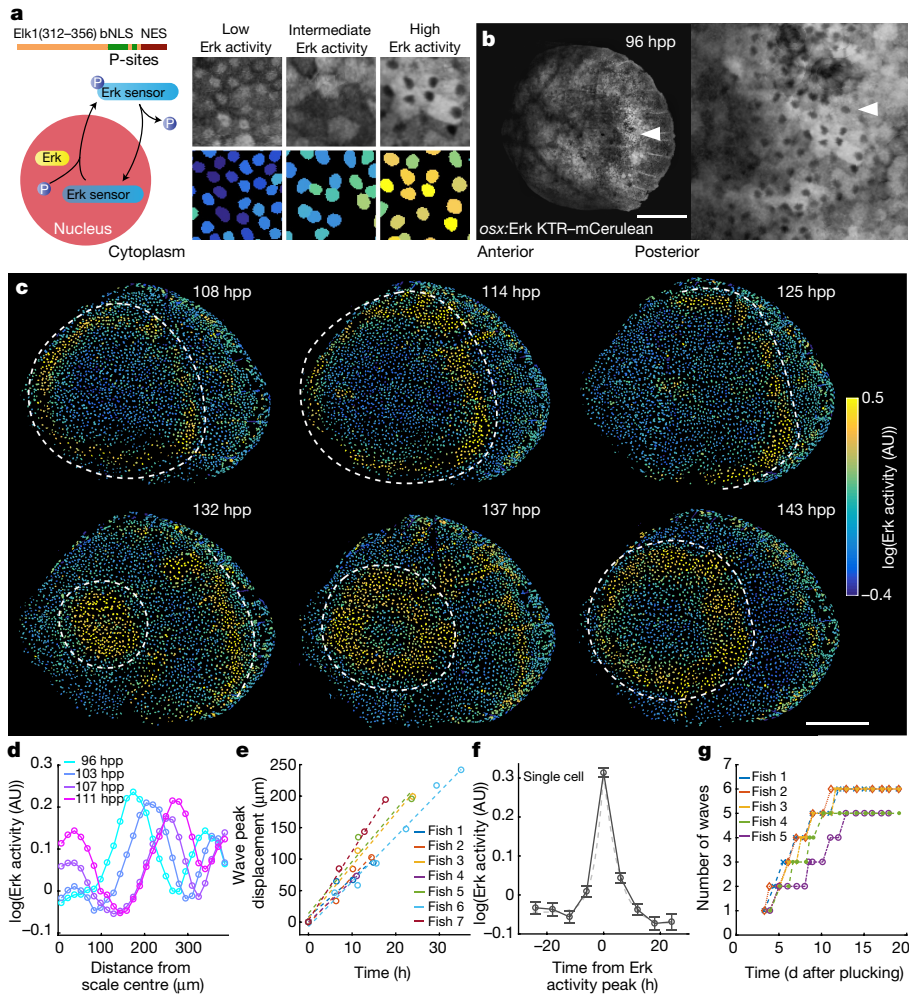


Fig. 2 | Waves of Erk activity travel across regenerating scales. **a**, Schematic of the Erk sensor (Erk KTR) (left). The mCerulean-tagged sensor includes a suboptimal bipartite nuclear localization sequence (bNLS) and a nuclear export sequence (NES). Erk binds to the sensor through its Elk1-derived docking site and phosphorylates it, favouring nuclear export (right) (quantified Erk activity in scale osteoblasts, represented as in c). P-sites, phosphorylation sites. **b**, Left, Erk KTR in a regenerating scale. Arrowheads, ring of cells in which Erk is active. $n > 50$ fish from >5 independent experiments. Right, magnification (image size, 150 μm). **c**, Quantification of Erk activity. $n > 50$ fish from >5 independent experiments. Dashed lines, front of active cells. Occasional activation can be observed along radii (vascularized and innervated

bone canals¹³). AU, arbitrary units. **d**, Example of a profile of a wave of Erk activity. **e**, Peak position of waves of Erk activity at 4–5 dpp. Dashed lines, linear fit; $n = 7$ scales from 7 fish pooled from 3 independent experiments. Peak width = $70 \pm 20 \mu\text{m}$ (Gaussian fit, ± 2 s.d.). **f**, Erk activity in tracked individual central osteoblasts located in the posterior of the scale. Error bars are mean with s.e.m.; $n = 89$ cells from 3 scales from 3 fish in a single trial; for each cell, $t = 0$ is peak Erk activity. Dashed lines, exponential fits of Erk activation and deactivation time (2.8 ± 0.5 h; 4.6 ± 0.6 h; 68% confidence interval). **g**, Cumulative number of waves of Erk activity as a function of time in individual regenerating scales measured longitudinally (single trial). Scale bars, 250 μm .

To further test quantitatively whether these features are sufficient in principle to generate waves, we developed a mathematical model of Erk signalling that involves a diffusible Erk activating signal and an Erk inhibitor, both generated by cells in which Erk is active (Fig. 3a). We found that a constant localized source can generate periodic waves of Erk activity (Fig. 3b, Extended Data Fig. 6a, Supplementary Video 3). In an alternative ‘phase wave’ model, Erk activity oscillates autonomously in each cell, and oscillation phases are organized in a graded spatial pattern such that Erk activity appears to travel across tissue. To distinguish between these scenarios, we analysed how Erk waves behave near an ablated region of scale tissue. Modelling predicts that phase waves travel across gaps, whereas trigger waves bend and turn around them (Fig. 3c, d). Laser ablation of small regions of regenerating scale tissue (Fig. 3c, d) revealed that Erk waves do not cross disrupted tissue, but instead curve and manoeuvre around it as expected for trigger waves.

The trigger wave model further predicts that wave speed depends on the time scale of self-sustained Erk activation¹⁶. This is likely to involve

protein synthesis, as wave propagation is impaired in fish that are treated with the translation inhibitor cycloheximide (Extended Data Fig. 6b, c). Modelling also predicts that the slowing of the Erk cascade will decrease wave speed (Fig. 3e). To test this prediction, we treated regenerating fish with different concentrations of the Mek inhibitor PDO325901, including concentrations that do not completely impair waves. The waves of Erk activity were indeed slowed by Mek inhibition in a dose-dependent manner (Fig. 3f, Extended Data Fig. 6d). Another prediction of the theory of trigger waves is that wave geometry influences their speed¹⁸. The speed v of a 2D wave depends on its radius of curvature R as $v = v_p - D/R$, in which v_p is the planar wave speed and D is the activator diffusivity; this means that small Erk waves are slower than larger ones. To test this prediction, we examined the small, developing scales of juvenile fish for patterns of Erk activity. We identified waves of Erk activity with diameters that were four times smaller than those of the regenerating scales of adult fish (Fig. 3g, Extended Data Fig. 6e). Wave speeds were slower than those of the regenerating scales of adult

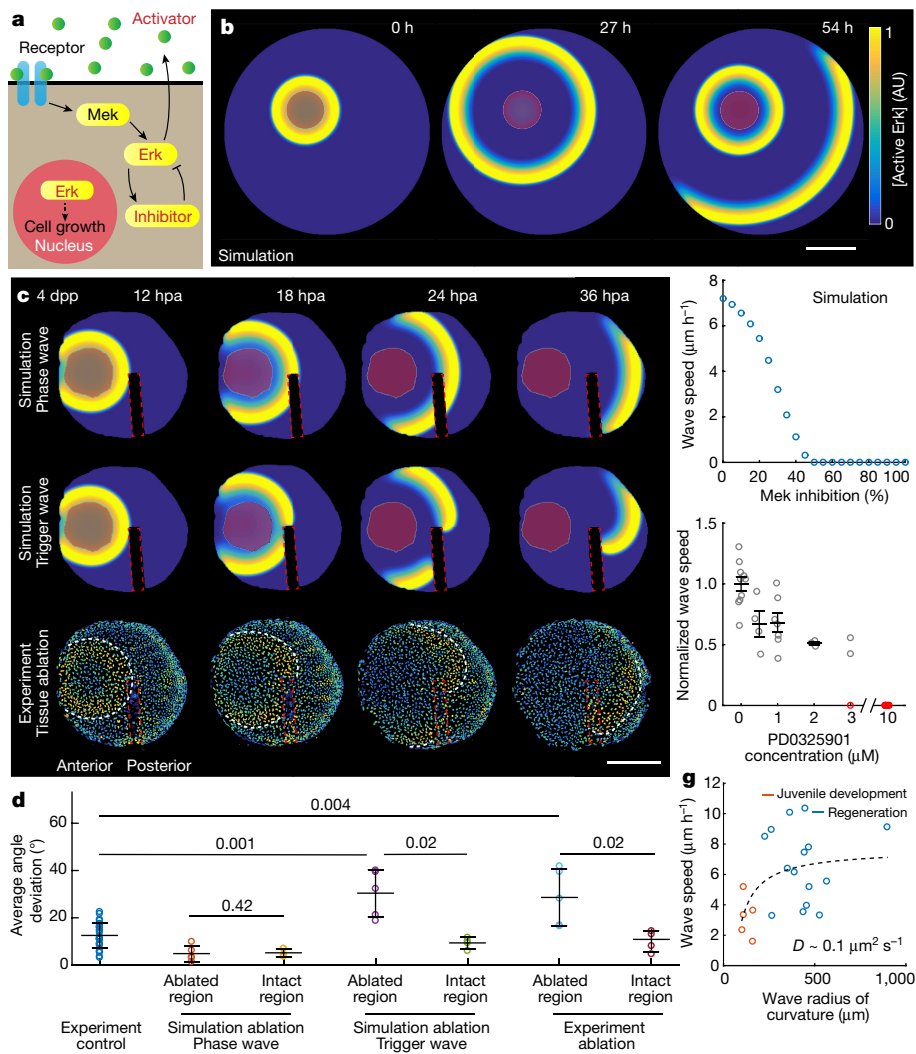


Fig. 3 | Erk activity propagates as a reaction-diffusion trigger wave. **a, b**, Model of Erk signalling dynamics, including a diffusible Erk activator (such as Fgf and/or another potential activator), a positive feedback between Erk and the activator, and a negative feedback that includes an Erk inhibitor. Red shaded region, constant source of activator. **c**, Erk activity in a scale in which a portion of the tissue has been ablated (red dashed line). Top and middle, mathematical model. Bottom, regenerating scales in which a portion of the tissue has been ablated by laser micro-surgery *in vivo*. White dashed line, wave front. For quantifications, see **d**. **hpa**, hours post-ablation. **d**, Wave-front angle with respect to a circular front. Error bars, mean with s.d.; control, $n=14$ scales from 13 fish pooled from 3 independent experiments; ablation, $n=6$ scales from 6 fish pooled from 2 independent experiments. Two-sided Wilcoxon's rank-sum test P is shown. **e**, Model prediction of the speed of the Erk wave for different levels of inhibition of the Erk activator Mek (waves at null speed are unstable). **f**, Wave speed corrected for tissue growth and normalized to respective control, in regenerating scales (4 dpp) in fish treated with different concentrations of the Mek inhibitor PD0325901. Error bar, mean with s.e.m. Circles, scales from individual fish, apart from 0 μM for which 10 scales from 9 fish were imaged; pooled independent experiments (left to right): 3, 1, 3, 1 and 2. Spearman's correlation coefficient -0.75 ; $P=2 \times 10^{-4}$. Red dots, Erk waves were completely impaired. **g**, Wave speed, corrected for tissue growth. Circles, individual scales from 12 (regenerating, pooled from 4 independent experiments) and 3 (juvenile, single trial) fish. Mean radius waves with s.e.m.; ontogeny, $130 \pm 10 \mu\text{m}$, regeneration, $440 \pm 40 \mu\text{m}$. Unpaired two-sided Student's t -test $P=5 \times 10^{-4}$. Mean wave speed with s.e.m.; ontogeny, $3.2 \pm 0.6 \mu\text{m h}^{-1}$, regeneration, $6.7 \pm 0.6 \mu\text{m h}^{-1}$. Unpaired two-sided Student's t -test, $P=0.009$. Model: $v=v_p - D/R$. Dashed line, model fit. Scale bars, 250 μm .

fish (Fig. 3g), consistent with the theoretical prediction. From this relationship between wave speed and curvature, we estimate the effective diffusivity of the signal that activates Erk to be about of $0.1 \mu\text{m}^2 \text{s}^{-1}$ (Fig. 3g). This value can be also obtained by another dimensional relationship. The speed of planar chemical waves is $v_p \sim (D/\tau)^{1/2}$, in which τ is the Erk activation time (a few hours) (Fig. 2f); as the planar wave speed is about $10 \mu\text{m h}^{-1}$, we infer again that D is about $0.1 \mu\text{m}^2 \text{s}^{-1}$. With this diffusion constant of the activator, our model generates trigger waves that traverse a millimetre-sized tissue in only a few days (Extended Data Fig. 6f, g, Supplementary Notes). Collectively, our observations argue that Erk activity spreads as excitable trigger waves.

To test whether Erk waves instruct patterns of tissue growth, we compared tissue expansion maps that were measured over time scales of several hours with maps of Erk signalling in the same individual regenerating scales. We found that the ring- or disc-like regions of tissue expansion correlate closely in space and time with Erk waves (Fig. 4a, b, Extended Data Fig. 7a–c). Moreover, tissue flows are strongly perturbed and tissue expansion rings are significantly reduced upon blockade of Erk activity with PD0325901 (Extended Data Fig. 7d–f).

Several waves traverse the entire scale over time periods of several days, and our findings predict that the extent of scale growth depends on the number of waves experienced by a given scale. By monitoring Erk activity for two weeks, we found that scale growth correlates with the generation of Erk waves—as the generation of Erk waves slows and stops, so does scale growth (Fig. 4c, d, Extended Data Fig. 7g, Supplementary Video 2). To further test this relationship, we perturbed

wave generation by a brief treatment with the Fgf receptor inhibitor BGJ398 (Fig. 4e, Extended Data Fig. 7h). After this transient block, Erk waves disappeared and were undetectable for around four days, and scale growth was concomitantly stalled. Subsequently, Erk waves re-emerged and scale growth resumed, with the same relationship between wave number and scale growth as in unperturbed regenerating scales (Fig. 4d). Collectively, these results argue that Erk waves direct osteoblast growth in both time and space.

To test whether regulation of Erk in the form of travelling waves is key for regeneration, we genetically modified the spatial pattern of Erk. Ectopic induction of an *fgf20a* transgene¹⁹ during the hypertrophic phase caused Erk activation in large portions (if not the entirety) of the population of scale osteoblasts. This tissue-wide activation was followed by global inactivation of Erk, ostensibly through negative feedback (Extended Data Figs. 4c, d, 8a, b). This perturbation, which we repeated daily for a week, impaired scale growth and caused modest morphological defects (Fig. 4f, Extended Data Fig. 8c–g). Similar experiments using *fgf3*²⁰ revealed similar—but less potent—effects on Erk activation and scale growth (Fig. 4f, Extended Data Figs. 4e, f, 9). Although our experiments do not exclude effects of *Fgf20a* or *Fgf3* that are independent of Erk, our observations suggest that travelling waves of Erk are favourable to spatially broad pulses of Erk activation for hypertrophic growth of scales, potentially as a means to limit accumulation of mechanical stresses. Indeed, a mathematical model that postulates feedback between growth and mechanical stress^{21–23} can capture the reduced scale growth when Erk is activated on a broader

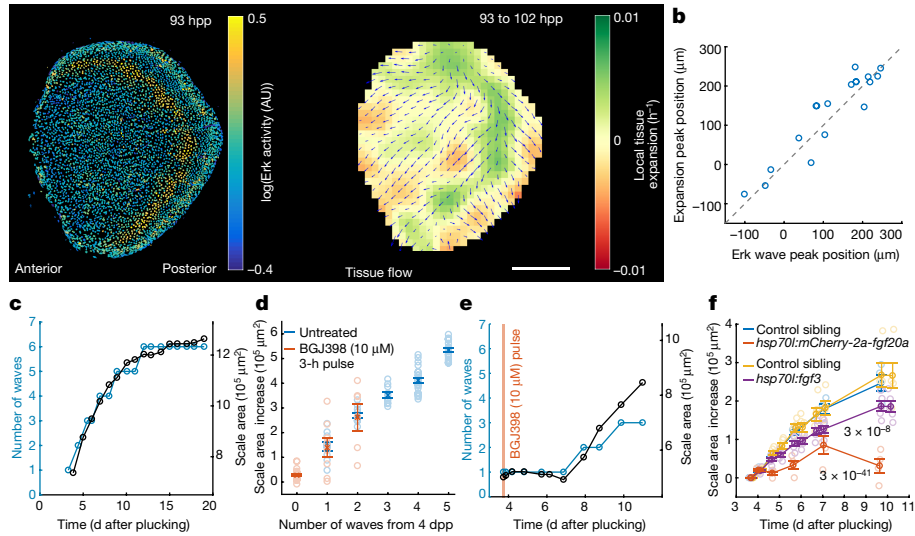


Fig. 4 | Waves of Erk activity direct tissue growth in regenerating scales.

a, Erk activity, tissue velocity field \vec{v} (tissue flow, blue arrows) and its divergence $\nabla \cdot \vec{v}$ (heat map). Quantifications in **b**. **b**, Expansion and Erk peak position. $n = 16$ scales from 12 fish pooled from >5 independent experiments. Pearson's correlation coefficient 0.93, $P = 2 \times 10^{-8}$. Dashed line, bisector of the axis. **c–e**, Cumulative number of waves and scale area during regeneration. Orange area, transient treatment with BGJ398. **d**, Area increase. Error bars, mean with s.e.m.; untreated, $n = 5$ scales from 5 fish in a single trial; BGJ398,

$n = 4$ scales from 4 fish pooled from 2 independent experiments. Partial Pearson's correlation coefficient calculated on averages and controlling for time, $\rho = 0.97$, $P = 2 \times 10^{-4}$. Untreated fish, same as in Fig. 2g, Extended Data Fig. 1c. **f**, Scale area increase in transgenic fish and respective control siblings not carrying the transgene. Error bars, mean with s.e.m.: *fgf20a* and control, 4 scales from 4 fish per condition in a single trial; *fgf3* and control, 5 scales from 5 fish per condition in a single trial (Extended Data Figs. 8, 9, Methods). Scale bar, 250 μm .

spatial range, as well as several geometric features of tissue growth (Extended Data Fig. 10, Supplementary Notes).

In summary, we report a mechanism for scale regeneration in zebrafish in which periodic waves of Erk activity orchestrate the collective behaviour of osteoblasts (Supplementary Video 4). Erk waves have previously been associated with cell migration during epidermal wound healing^{24–26} and with cellular contractility during tissue invagination²⁷. Here, we reveal Erk waves as a mechanism to coordinate growth during regeneration. We propose that repeated waves of transmitted signals can serve as a mechanism of organizing cell behaviours within large regenerating tissues, and that wave properties such as number, speed and geometry can determine how injured organs and appendages recover their size and shape.

Online content

Any methods, additional references, Nature Research reporting summaries, source data, extended data, supplementary information, acknowledgements, peer review information; details of author contributions and competing interests; and statements of data and code availability are available at <https://doi.org/10.1038/s41586-020-03085-8>.

1. Gelens, L., Anderson, G. A. & Ferrell, J. E. Jr. Spatial trigger waves: positive feedback gets you a long way. *Mol. Biol. Cell* **25**, 3486–3493 (2014).
2. Hubaud, A., Regev, I., Mahadevan, L. & Pourquié, O. Excitable dynamics and Yap-dependent mechanical cues drive the segmentation clock. *Cell* **171**, 668–682 (2017).
3. Werner, S., Vu, H. T. & Rink, J. C. Self-organization in development, regeneration and organoids. *Curr. Opin. Cell Biol.* **44**, 102–109 (2017).
4. Sonnen, K. F. et al. Modulation of phase shift between Wnt and Notch signaling oscillations controls mesoderm segmentation. *Cell* **172**, 1079–1090 (2018).
5. Deneke, V. E. & Di Talia, S. Chemical waves in cell and developmental biology. *J. Cell Biol.* **217**, 1193–1204 (2018).
6. Chara, O., Tanaka, E. M. & Bruschi, L. Mathematical modeling of regenerative processes. *Curr. Top. Dev. Biol.* **108**, 283–317 (2014).
7. Di Talia, S. & Poss, K. D. Monitoring tissue regeneration at single-cell resolution. *Cell Stem Cell* **19**, 428–431 (2016).
8. Aman, A. J., Fulbright, A. N. & Parichy, D. M. Wnt/β-catenin regulates an ancient signaling network during zebrafish scale development. *eLife* **7**, e37001 (2018).
9. Bereiter-Hahn, J. & Zylberberg, L. Regeneration of teleost fish scale. *Comp. Biochem. Physiol. Part A. Physiol.* **105**, 625–641 (1993).
10. Cox, B. D. et al. In toto imaging of dynamic osteoblast behaviors in regenerating skeletal bone. *Curr. Biol.* **28**, 3937–3947 (2018).
11. Iwasaki, M., Kuroda, J., Kawakami, K. & Wada, H. Epidermal regulation of bone morphogenesis through the development and regeneration of osteoblasts in the zebrafish scale. *Dev. Biol.* **437**, 105–119 (2018).
12. Sire, J. Y., Allizard, F., Babiar, O., Bourguignon, J. & Quilhac, A. Scale development in zebrafish (*Danio rerio*). *J. Anat.* **190**, 545–561 (1997).
13. Rasmussen, J. P., Vo, N. T. & Sagasti, A. Fish scales dictate the pattern of adult skin innervation and vascularization. *Dev. Cell* **46**, 344–359 (2018).
14. Pasqualetti, S., Banfi, G. & Mariotti, M. The zebrafish scale as model to study the bone mineralization process. *J. Mol. Histol.* **43**, 589–595 (2012).
15. Regot, S., Hughey, J. J., Bajer, B. T., Carrasco, S. & Covert, M. W. High-sensitivity measurements of multiple kinase activities in live single cells. *Cell* **157**, 1724–1734 (2014).
16. Murray, J. D. *Mathematical Biology*, 3rd edn (Springer, 2002).
17. Lake, D., Corrêa, S. A. & Müller, J. Negative feedback regulation of the ERK1/2 MAPK pathway. *Cell. Mol. Life Sci.* **73**, 4397–4413 (2016).
18. Tyson, J. J. & Keener, J. P. Singular perturbation-theory of traveling waves in excitable media. *Physica D* **32**, 327–361 (1988).
19. Shibata, E. et al. Fgf signalling controls diverse aspects of fin regeneration. *Development* **143**, 2920–2929 (2016).
20. Sweet, E. M., Vemaraju, S. & Riley, B. B. Sox2 and Fgf interact with Atoh1 to promote sensory competence throughout the zebrafish inner ear. *Dev. Biol.* **358**, 113–121 (2011).
21. Shraiman, B. I. Mechanical feedback as a possible regulator of tissue growth. *Proc. Natl Acad. Sci. USA* **102**, 3318–3323 (2005).
22. Basan, M., Risler, T., Joanny, J. F., Sastré-Garaux, X. & Prost, J. Homeostatic competition drives tumor growth and metastasis nucleation. *HFSP J.* **3**, 265–272 (2009).
23. Irvine, K. D. & Shraiman, B. I. Mechanical control of growth: ideas, facts and challenges. *Development* **144**, 4238–4248 (2017).
24. Hiratsuka, T. et al. Intercellular propagation of extracellular signal-regulated kinase activation revealed by *in vivo* imaging of mouse skin. *eLife* **4**, e05178 (2015).
25. Aoki, K. et al. Propagating wave of ERK activation orients collective cell migration. *Dev. Cell* **43**, 305–317 (2017).
26. Hino, N. et al. ERK-mediated mechanochemical waves direct collective cell polarization. *Dev. Cell* **53**, 646–660 (2020).
27. Ogura, Y., Wen, F. L., Sami, M. M., Shibata, T. & Hayashi, S. A switch-like activation relay of EGFR-ERK signaling regulates a wave of cellular contractility for epithelial invagination. *Dev. Cell* **46**, 162–172 (2018).

Publisher's note Springer Nature remains neutral with regard to jurisdictional claims in published maps and institutional affiliations.

© The Author(s), under exclusive licence to Springer Nature Limited 2021

Methods

Fish husbandry, scale injury and pharmacological treatments

Zebrafish of Ekkwill, Ekkwill/AB and AB strains were maintained between 26 and 28.5 °C with a 14:10 h light:dark cycle. Fish between 3 and 18 months old were used for experiments. To assess regenerating scales in *hsp70l:dnfgfr1-eGFP;osx:ErkKTR-mCerulean;osx:H2A-mCherry* fish, approximately 9-week-old fish were used. To assess developing scales in juvenile fish, fish at the squamation stage were used (about 4 weeks old). Scale plucking was performed essentially as previously described¹⁰. In brief, fish were anaesthetized in 0.09% phenoxyethanol (Sigma L77699) in system water until swimming ceased and operculum movement slowed. Then, they were placed in a Petri dish, and fluorescent scales were viewed under a fluorescence dissecting microscope. Three rows of 7–15 scales were plucked with forceps from the trunk of the fish, starting from the caudal peduncle and proceeding anteriorly. After scale removal, fish were returned to system water to recover from anaesthesia. No statistical methods were used to predetermine sample size. Fish, mixed males and females, were randomly allocated in control and experimental groups. When possible, siblings were used for control and experimental groups. It was not possible to blind investigators during data collection, because fish from control and experimental groups can be distinguished by cell behaviours and/or fluorescent reporters. However, data quantification was performed automatically using the same computational algorithm. When necessary, human manual data curation was performed by blinded researchers, although often data from control and experimental groups can be recognized from phenotypes. Researchers were not blinded during data visualization. All fish experiments were approved by the Institutional Animal Care and Use Committee at Duke University and followed all the relevant guidelines and regulations.

Transgenic lines used in this study were: Tg(*osx:H2A-mCherry*)^{pd310} (ref.¹⁰), Tg(*hsp70l:dnfgfr1-EGFP*)^{pd1} (ref.²⁸), Tg(*osx:EGFP-CAAX*)^{pd51} (ref.²⁹), Tg(*osx:mCherry-zCdt1*)^{pd270} (ref.¹⁰), Tg(*osx:Venus-hGemini*)^{pd271} (ref.¹⁰), Tg(*osx:ErkKTR-mCerulean*)^{pd2001} (this Article), Tg(*osx:H2A-mEos2*)^{pd2002} (this Article), Tg(*hsp70l:mCherry-2a-fgf20a*)¹⁹ and Tg(*hsp70l:fgf3*)^{x27} (ref.²⁰).

Construction of transgenic zebrafish

H2A-mEos2 and *ErkKTR-mCerulean* were subcloned by ligation and/or Gibson assembly into a pBluescript SK plasmid, modified to contain ISceI sites flanking the multicloning site and containing the *osx* regulatory sequence, derived from an *osx:H2A-mCherry* plasmid¹⁰. The *ErkKTR* sequence was derived from a pENTR-ErkKTR-Clover plasmid gifted by M. Covert (Addgene plasmid no. 59138; <http://n2t.net/addgene:59138>; RRID: Addgene_59138); the *mCerulean* sequence from a Cdk1 FRET sensor gifted by J. Pines (Addgene plasmid no. 26064; <http://n2t.net/addgene:26064>; RRID: Addgene_26064); and the *mEos2*³⁰ sequence from mEos2-CytTERM-N-17 plasmid gifted by M. Davidson (Addgene plasmid no. 57366; <http://n2t.net/addgene:57366>; RRID: Addgene_57366).

Plasmids were linearized using ISceI enzyme (NEB R0694S; final concentration: 0.33 U μ l⁻¹) for 30 min at 37 °C before injection into AB or EK embryos at the one-cell stage. Plasmids and plasmid sequences are available upon request to the corresponding authors.

Heat-shock and pharmacological treatments

Heat-shocks were performed essentially as previously described²⁸. Fish were placed in an aquarium system with recirculating water that maintained 26–28.5 °C water for all but the 1.75 h during which the water was heated to 38 °C. Water was allowed to return to temperature for at least 2 h before imaging.

In Fig. 4f, Extended Data Figs. 2b, 4c–f, 8a, b, e–g, 9, fish were heat-shocked every day at the same time starting at 4 dpp. In the case of *dnfgfr1* (encoding a dominant-negative form of Fgfr1 (*fgfr1* is also

known as *fgfr1a*)) expression in Extended Data Fig. 2b, fish were imaged after (>4 h) the start of each heat-shock. In the case of *fgf3* overexpression in Fig. 4f, Extended Data Figs. 4e, f, 9, scales were imaged before and after heat-shock; imaging times are shown in Extended Data Fig. 9b). In the case of *fgf20a* overexpression in Fig. 4f, Extended Data Figs. 4c, d, 8a, b, e–g, fish were imaged before (<6 h) and after (>4 h) the start of heat-shock at 4 dpp, and imaged before (<6 h) or after (>4 h) the start of heat-shock on the following days.

In the case of *dnfgfr1* in Extended Data Fig. 4a, b, fish were imaged before (<6 h) and 7–10 h after the start of heat-shock.

In Extended Data Fig. 10j (first heat-shock), fish were heat-shocked at about 3.5 dpp and imaged thereafter every 3 h for around 9 h. In Extended Data Figs. 8c, d, 10j (second heat-shock) fish were heat-shocked at about 3.5 dpp and about 4.5 dpp and imaged after the second heat-shock every 3 h for around 12 h. In the case of PD0325901 (10 μ M) treatment followed by *fgf20a* overexpression (Extended Data Fig. 10j–l), fish were treated at 4 dpp for 24 h with PD0325901 (10 μ M). Then, they were transferred to fresh water, heat-shocked, returned to the chemical treatment and imaged every 3 h for about 9 h. For testing whether the protocol can activate Erk (Extended Data Fig. 10k), fish were imaged after heat-shock (>4 h).

In each heat-shock experiment, *hsp70l:mCherry-2a-fgf20a*, *hsp70l:fgf3* or *hsp70:dnfgfr1-eGFP* fish were heat-shocked in the same tank and at the same time together with their respective control sibling that did not carry the transgenes. In each fish, the same scale was recognized at different time points from its position in the scale array. The correspondence between fish at different time points was determined after imaging by scale similarity.

For pharmacological treatments, fish were first imaged and then were immersed in the pharmacological compound diluted to working concentration in fish water for the duration of the treatment (BGJ398 (Selleck-Chem S2183); cycloheximide (Sigma-Aldrich 01810); JNJ-42756493 (Selleck Chem S8401); PD0325901 (Selleck Chem S1036); PD153035 (Selleck-Chem S6546); and SU5402 (Selleck-Chem S7667). PD153035 is an inhibitor of Egf receptors that is known to be effective in adult zebrafish^{31,32}. Fish were maintained off the aquarium system in the dark. Treatment medium was changed roughly every 12 h. In the case of BGJ398 transient treatment (Fig. 4d, e, Extended Data Fig. 7g), scales were treated for around 3 h at 4 dpp and transferred to fresh water afterwards. Fish were fed before changing treatment medium. In each fish, the same scale was recognized at different time points from its position in the scale array. The correspondence between fish at different time points was determined before imaging by fish similarity or after imaging by scale similarity. In each experiment, control fish (siblings, when possible) were treated with the same concentration of DMSO vehicle as the treated group and imaged during the same day (when possible (otherwise, within weeks)).

Laser-mediated photoconversion

For H2A-mEos2 photoconversion, we used the same confocal-based setup as described in ‘Live imaging’; H2A-mEos2 was converted by scanning repeatedly a small region of interest around a single nucleus with a 405-nm laser during the proliferative (3 dpp) or hypertrophic (4 dpp) phases; several nuclei (around ten) were converted per scale. Scales bearing photoconverted nuclei were imaged daily during the following days. Nuclei were tracked manually and instances of cell division were scored manually. Photoconversion images shown in Extended Data Fig. 1 were adjusted differently to compensate for different nuclear brightness immediately after photoconversion and days afterwards.

Laser microsurgery

Tissue ablation was performed using a Zeiss PALM MicroBeam 4.2 microsurgery setup (objective 10 \times 0.25 NA Fluar, 20140-9900) including a Zeiss Axio Observer Z1 microscope for tissue visualization. Tissue ablation was performed along a manually selected path covering a rectangular

region, roughly 50–300 μm × 50 μm, with a 355-nm pulsed laser (pulse energy > 90 μJ, pulse duration < 2 ns, pulse frequency 1–100 Hz).

Live imaging

In vivo confocal imaging was performed as previously described¹⁰. A zebrafish was anaesthetized in 0.01% tricaine (Sigma E10521-50G) in system water and transferred to a 1% agarose bed in an acrylic glass plate. The caudal fin of the fish was set on a glass slide to bring the caudal peduncle of the trunk parallel with the platform, and diluted tricaine was placed near the head of the fish. Cooling 1% agarose was applied on the caudal fin, the trunk anterior to the imaged scale, and the areas of platform dorsal and ventral to the scale. Then, fish were immersed in diluted tricaine. Gill movements were monitored visually and, when they slowed, system water was applied using a peristaltic pump (Cole Parmer; no. EW-73160-32; silicon tubing: Tygon, 0.7 mm inner diameter and 2.4 mm outer diameter, B-44-4X) until regular rhythm was restored (3.5 ml per min flow rate). In each fish, the same scale was recognized at different time points from its position in the scale array. After imaging, a system water flow was applied using the peristaltic pump, until gill movement quickened. Then, the fish was returned to system water. For longitudinal time courses, fish were mounted, imaged and then returned to system water at each time point. Fish were imaged at variable intervals of approximately 3, 6, 12, 24, 48 or 72 h.

Confocal images were acquired using a Leica SP8 confocal microscope and LAS X 2.01.14392 software, with a HC FLUOTAR L 25×/0.95 W VISIR water immersion lens (Leica 15506374) at 0.75× zoom. As scales are larger than the field-of-view of our microscopy setup, they were imaged with multiple overlapping z-stacks (1–9 with variable number of planes) to cover the entire osteoblast tissue. High-resolution images were acquired at 1,024 × 1,024 resolution (0.606 μm pixel size) and a z-step of 0.606 μm. Scale area in *hsp70l:dnfgfr1-eGFP* fish and control siblings was measured using low-resolution images at 512 × 512 resolution (1.212 μm pixel size) and a z-step of 1.2 or 1.7 μm. Fluorescent proteins were imaged using the following lasers: ErkKTR-mCerulean, 458 nm; unconverted H2A-mEos2, 488 nm; converted H2A-mEos2, 561 nm; Venus-human (h)Geminin, 488 or 514 nm; eGFP-CAAX, 488 nm; Dnfgfr1-eGFP, 458 or 488 nm; H2A-mCherry, 561 nm; and mCherry-zebrafish (z)Cdt1, 561 nm. A variable laser power was used depending on the expression of the transgenic reporters.

ErkKTR-mCerulean in *hsp70l:dnfgfr1-eGFP* fish was imaged using a 458 nm laser and restricting the collected emitted spectrum to minimize Dnfgfr1-eGFP bleed-through with respect to ErkKTR-mCerulean signal. Control experiments showed that Dnfgfr1-eGFP signal corresponded to 5% of mCerulean signal, and thus did not bias Erk activity measurements in a major way.

A Zeiss AxioZoom V16 and Zen Pro 2012 software was used to acquire illustrative low-magnification images (Extended Data Fig. 1a). In this case, fish were anaesthetized in 0.01% tricaine in system water and transferred to a Petri dish with their heads partially submerged in diluted tricaine. Fish were imaged quickly and then returned to system water.

EdU incorporation

Ten μl of 10 mM EdU (Tokyo Chemical Industry E1057) in PBS was injected intraperitoneally at 1.5 and 4.5 dpp. Regenerated scales were collected at 4.5 dpp or 6.5 dpp and fixed in 4% formaldehyde (Sigma-Aldrich L2525249). EdU was detected using the Click-&-Go EdU AF 488 Imaging Kit (Click Chemistry Tools no. 1324).

Osteoblast dissociation and sorting, and RNA extraction and sequencing

Scale regeneration was induced by plucking about 50 scales, in 3 rows, from each side of *osx:H2A-mCherry* or *osx:Venus-hGeminin* fish. At 4 dpp, all regenerating scales were plucked as described in ‘Fish husbandry,

scale injury and pharmacological treatments’ and collected in PBS on ice. Three to five fish were used per sample. Tissue was pelleted by centrifugation (5 min at 600g) and resuspended in 600 μl of 13 U ml⁻¹ Liberase (DH-Research Grade, Sigma no. S401054001) in HBSS (Gibco no. 14025-092) and incubated at 37 °C for 1 h. Every 15 min, 500 μl of supernatant was removed, quenched with 65 μl sheep serum (Sigma S2263) on ice and 500 μl of fresh liberase was added to the primary tube. All collected supernatant was filtered using 50 μm filters (Corning no. 431750), pelleted (5 min at 600g) and resuspended in 1 ml DMEM + 1% BSA (UltraPure - Invitrogen AM2616). Before sorting, 1 μg ml⁻¹ DAPI (Sigma D9542) was added to the tube.

Cells were analysed and sorted using a SH800S Sony Cell Sorter using a 100 μm disposable chip. Initially, events were gated using forward versus side scatter areas (488 nm laser). Then, single cells were enriched by gating forward scatter height versus forward scatter area (488 nm excitation laser). Live cells were enriched by selecting a population with low DAPI emission (405 nm excitation laser). Finally, H2A-mCherry⁺Venus-hGeminin⁻ (D in Extended Data Fig. 5f) and H2A-mCherry⁺Venus-hGeminin⁺ (E in Extended Data Fig. 5f) were sorted by gating Venus-hGeminin (488 nm excitation laser) versus H2A-mCherry (561 nm excitation laser). Cells were collected in PBS or TriReagent (Sigma T9424). RNA was extracted using TriReagent followed by RNAeasy microKit (Qiagen no. 74004).

Library preparation was performed by BGI Genomics (Low Input Library Preparation, BT01). Sequencing was performed by BGI Genomics using their BGISEQ-500 platform (paired end, 100 bp per read and 40 million clean reads per sample).

Gene expression analyses by RNA sequencing

Reads were trimmed using Trim Galore (0.4.1, with -q 15--paired) and then mapped with TopHat³³ (v.2.1.1, with parameters --b2-very-sensitive --no-coverage-search and supplying the UCSC danRer10 refSeq annotation). Gene-level read counts were obtained using the featureCounts³⁴ (v.1.6.1) by the reads with MAPQ greater than 30. The Bioconductor package DESeq2³⁵ (v.1.26.0) was used for differential expression analysis. Gene set enrichment analysis^{36,37} (Supplementary Table 1) was used to define the enriched gene set for the prereduced *Homo sapiens* homologues list by Wald statistics.

Scale RNA extraction and quantitative real-time PCR

Scale regeneration was induced by plucking about 50 scales, in 3 rows, from 1 side of *osx:H2A-mCherry* or *osx:H2A-mCherry* *hsp70l:dnfgfr1-eGFP* fish. Two fish were used per sample. In the case of PD0325901 treatment, fish were treated for around 9 h with PD0325901 (10 μM) or control DMSO vector at 4 dpp; then, whole regenerating scales were plucked and collected in TriReagent on ice. In the case of *dnfgfr1* expression, fish were heat-shocked as described in ‘Heat-shock and pharmacological treatments’; then, whole regenerating scales were plucked about 11 h after the start of the heat-shock (therefore, about 9 h after reaching maximum temperature) and collected in TriReagent (Sigma T9424). The tissue RNA was extracted using TriReagent followed by RNAeasy microKit (Qiagen no. 74004). Quantitative PCR was performed on a Roche LightCycler 480 with Software release 1.5.0 SP4 using LightCycler 480 SYBR Green I Master Mix (Roche 04707516001) with the following primers: *actb2* forward (fwd): GACAACGGCTCCGGTATG, reverse (rev): CATGCCAACCATCACTCC³⁸; *spry4* fwd: GCGGAGCAGCCAAGAT ACT, rev: CAGGCAGGGCAAACCAATGAG³⁹; *dusp2* fwd: AGCCATCC ACTTCATTGATTG, rev: TGGCCCATGAATGCGAGATT; and *dusp5* fwd: ACTTTGTCCGACTTGACGAG, rev: TGGGTTTCATGATGTACGC⁴⁰. Amplification was performed in technical triplicates and transcript expression levels were normalized to *actb2* as a control. Transcript fold change was calculated with respect to the corresponding control using the ΔΔC_p method⁴¹, in which C_p is the maximum of the second derivative of the fluorescence-cycle curve, calculated using the Roche LightCycler 480 software.

Data analysis

Image processing and data analysis were performed with custom-written MATLAB (Mathworks) 2016b software, unless stated otherwise. Each acquired z-stack contains a portion of scale, positioned diagonally with respect to the x–y plane, and several overlapping neighbouring scales. Each scale includes a monolayer of hyposquamal osteoblasts on the dermal side (the subject of this study), and a sparse population of episquamal osteoblasts on the epidermal side. Therefore, several image processing steps are required to isolate the hyposquamal layer for quantification.

First, z-stacks covering different portions of a scale were stitched in a single z-stack using a custom-written 3D stitching software based on image cross-correlation. Then, z-stacks were rotated to position the entire osteoblast tissues as parallel as possible to the x–y axes (here and hereafter, H2A–mCherry nuclear signal was used as nuclear osteoblast reference; in *osx:Venus-hGeminin* *osx:mCherry-zCdt1* fish, the Venus–hGeminin and mCherry–zCdt1 signals were combined and used as nuclear osteoblast markers instead). Overlapping neighbouring scales were computationally removed by computationally assisted manual data curation. Once neighbouring scales were removed, the z-stack was rotated again to position the isolated scale as parallel as possible to the x–y axes. Then, the osteoblast tissue was segmented using intensity-based thresholding and morphological operations. Scales were computationally flattened so that the dermal side of the segmented osteoblast tissue was at the same z-position. To isolate the hyposquamal population, a z-slice was computationally isolated from the dermal side of the flattened scale. To determine the thickness of the hyposquamal z-slice, the total intensity z-profile of the flattened osteoblast tissue (nuclear signal) was calculated. Because the hyposquamal tissue contains the majority of osteoblasts in 4 dpp to mature scales, its centroid corresponds roughly to the peak of the nuclear-signal z-intensity profile. Therefore, the hyposquamal slice was taken from the dermal side of the flattened scale to the peak of the total-intensity z-profile (a thicker slice would include cells from the episquamal layer). For the purpose of nuclei segmentation and visualization, z-stacks were equalized by contrast-limited adaptive histogram equalization.

For osteoblast counting and Erk activity quantification, nuclei were segmented by TGGM software⁴² using the equalized hyposquamal nuclear signal (H2A–mCherry or combined Venus–hGeminin and mCherry–zCdt1 signal). For Erk quantification, a mask corresponding to each nucleus was drawn using nuclei segmentation; the nuclear mask was dilated and the difference of the dilated mask and the nuclear mask was taken as a cytoplasmic mask. Then, average Erk KTR–mCerulean fluorescence was calculated in the nuclear and cytoplasmic regions. Erk activity was measured as the ratio of cytoplasmic and nuclear average Erk KTR–mCerulean fluorescence levels. A similar procedure, but using Venus–hGeminin and mCherry–zCdt1, was applied to calculate the normalized Venus–hGeminin and mCherry–zCdt1 signal (Extended Data Fig. 5). In these instances, each signal was also normalized by the corresponding laser power.

Erk activity profiles were calculated by averaging Erk activity along a 240 µm-wide stripe passing through the source of Erk waves (manually selected) and the centroid of the osteoblast tissue. For visualization purposes, Erk activity profiles were smoothed using a Savitzky–Golay filter. The position and height of the wave peak was fitted from the unsmoothed 1D Erk activity profile using a quadratic function around a manually selected initial peak point. Wave speed was calculated from wave peaks that were located away from the source, thus around or past the centroid of the scale, and that had not yet reached the scale external rim. As waves travel at the same time as tissue grows, wave speed may include a component attributable to the growth on the underlying tissue. To compensate for this effect, we calculated a corrected wave velocity (Supplementary Methods), assuming that the overall tissue was growing by an affine deformation centred in the scale centroid. Similar

conclusions are drawn whether the total or corrected wave velocity are considered. In Extended Data Fig. 10i, the 1D Erk-activity profile is smoothed and the inverse of its second derivative is calculated. The position of each trough is measured as for Erk activity peaks.

For the calculation of Erk wave-front bending in tissue ablation experiments (Fig. 3c, d), as osteoblasts gradually repopulate the wound induced by the laser, only scales in which the Erk wave passed partially or entirely the ablated region before it had healed were used for quantification. To quantify the induced deformations of the wave front, we computed the angle between the normal to the Erk wave front at a given point and the line connecting the wave centre to the same point on the wave front (this angle would be zero for a perfectly concentric wave). ‘Ablated region’ angles are the average of the angles computed using lines passing through the ablated region, and ‘intact region’ angles are the averages of the angles computed using lines not passing through the ablated region. In experimental images, the position of the Erk wave front was manually selected (>25 point per wave); in simulations, the location of the wave was extracted by thresholding and skeletonizing 2D Erk-activity maps. As wave velocity is different in each experiment and stochastically fluctuating between experimental time points, each wave front in experimental time points was compared to the wave front in the most similar simulation time point, chosen independently for trigger and phase wave simulations. Maximum similarity between experimental and simulated time points was computed by minimizing a discrepancy score computed as follows: the experimental and simulated wave fronts were discretized in space, each discrete point on the experimental wave front was matched to the closest points in the simulated wave front and distances between wave front couples were calculated; the discrepancy score between two experimental and simulated time-points was computed as the average of the wave front distances. The same procedure was applied to match and compare wave fronts in the trigger and phase wave simulation.

For quantification of Erk inhibition in pharmacologically or genetically perturbed scales, the relative amplitude of an Erk peak was measured before and after treatment (Supplementary Methods). When a clear wave peak was absent owing to Erk inhibition, the Erk value was measured in a region similar to where the Erk peak was before inhibition. For quantification of Erk overactivation in scales overexpressing *fgf20a* or *fgf3*, the total number of Erk-active cells was counted automatically (cytoplasmic Erk KTR signal >1.1 nuclear Erk KTR signal).

The number of waves in Figs. 2g, 4c–e, Extended Data Fig. 7g, h was counted manually examining quantified Erk activity maps. Scale area was measured by manually selecting the scale region from raw images or from the isolated hyposquamal layer. Average cell area is calculated as the inverse of cell density. Cell density is measured by counting the number of nuclei in a central circular region (in Extended Data Fig. 1c, only the posterior portion of the circle was taken, as nuclei become too dim to be quantified reliably in the anterior region past 10 dpp) and dividing by the area of the region.

For EdU quantification, a similar procedure was used as for Erk activity quantification. The hyposquamal layer was isolated computationally and a region containing only central osteoblasts in intact fixed tissue was manually selected. The transgenic H2A–mCherry marker was used to segment nuclear masks by TGGM software⁴². Average EdU–AFDye 488 Azide signal was measured in each nucleus using the segmented nuclear mask and normalized by the average background signal, measured in the surrounding cytoplasm using a cytoplasmic mask. A nucleus was considered EdU⁺ when the normalized nuclear signal was higher than 1.6.

For the detection of converted mEos2 nuclei, the hyposquamal layer was segmented using the unconverted mEos2 signal. Then, converted mEos2 cells were manually selected and counted.

For the calculation of tissue flows, osteoblast nuclei (equalized H2A–mCherry marker, hyposquamal layer) were segmented and then tracked using Illastik 1.3.3 software⁴³. Nuclei velocities were calculated

between frames 6 to 15 h apart, and the overall tissue flow was calculated by averaging individual nuclei velocities in 30 μm -sized squared regions. Tissue flow maps were smoothed by an averaging filter (size of 60 μm); tissue flow 2D velocity two-point correlator was calculated using the unsmoothed velocity field; the exponential fit was performed excluding the first point, which reflects flow velocity variance. Two-dimensional divergence and curl (that is, vorticity) of the tissue flow map were calculated using built-in MATLAB functions and smoothed by a Gaussian filter (s.d., 91 μm ; size, 152 μm). The position of the expansion and compression peak and trough were measured as in the case of the position of the Erk activity peak. When the expansion region was organized in a disc instead of a ring, the external edge of the expansion ring was selected. To calculate the normalized total expansion rate, the scale was divided in squared regions (size of 30 μm), the expansion rate of expanding regions was summed and divided by the total number of regions throughout the scale.

To calculate scale morphology deviation, the boundary of each scale was manually selected. The boundary was transformed by a uniform dilation such that the average distance of the boundary from its centroid was unitary for each scale. Then, the boundary was expressed in polar coordinates and the morphology deviation was calculated as the average deviation of the radial coordinates between each time point and the one before the first heat-shock.

Mathematical modelling

The biological model of Erk propagation is based on a positive feedback loop between Erk and its diffusible activator (such as Fgf), and a negative feedback loop between Erk and its inhibitor (Fig. 3a). In brief, diffusible extracellular activator binds to its receptor and triggers a signalling cascade that leads to the activation of Erk. Active Erk increases the production and/or stimulates the diffusible activator, thus generating a self-sustaining positive feedback loop that can activate neighbouring cells. Active Erk activates its own inhibitor, thus generating a delayed negative feedback loop.

This chemical network was described mathematically as a reaction–diffusion system that was simulated using the finite differences method⁴⁴. The model includes three variables: the concentration of the Erk activator (such as a growth factor ligand) (A), the fraction of active Erk (E) and the cellular concentration of the Erk inhibitor (I). The activator diffuses with a diffusion constant D , and the inhibitor and Erk are assumed to not diffuse. The positive feedback between activator concentration and fraction of active Erk is described by a sigmoidal function. Mass action inactivation terms were used for the feedback between Erk activity and inhibitor concentration. In addition, all species degrade or inactivate with first-order kinetics. The activator and the inhibitor are produced at rates proportional to the fraction of active Erk. In addition, the activator is produced at a constant rate in a ‘source’ region located in the anterior half of the scale. The system of equations, parameter definitions and values are reported in the Supplementary Methods. The simulation domain is a 1,090 \times 1,090 μm square (simulation grid size of 2 μm) in the standard simulation. A large portion of the simulation domain is the scale region. In the standard simulation, the scale region is a disc that is 520 μm in radius, with the surrounding region representing the extracellular space between the scale and other tissues. Erk activity and inhibitor concentrations are null outside the scale region. The activator diffuses outside the scale, but absorbing boundary conditions are set at the domain boundary; the activator degradation length is about 8 μm (Supplementary Methods), which is smaller than the minimum distance between the scale and the simulation domain boundary (>25 μm). The initial condition is that Erk, activator and inhibitor are set to zero.

The simulation time step in the standard simulation is 0.005 h. A phase wave and a trigger wave simulation are performed for each ablation experiment. The domain size in this case is 1,515 \times 1,515 μm (simulation grid size of 3 μm); for each simulation, the scale, source and

ablated region sizes are set to match the corresponding experiment. In the trigger wave simulation, Erk and the inhibitor are set to zero in the ablated region, whereas the activator can diffuse freely in that region; in the phase wave simulation, as tissue ablation should not influence system dynamics, Erk, activator and inhibitor are set equal to the same quantities in a trigger wave simulation in which no region was ablated.

Reporting summary

Further information on research design is available in the Nature Research Reporting Summary linked to this paper.

Data availability

Reagents are available upon request. Transcriptomics data are available from Gene Expression Omnibus (GEO) under accession number GSE147551. The microscopy dataset consists of large files (>1 Tb); therefore, microscopy data are available from the corresponding authors, without limitation. Source data are provided with this paper.

Code availability

Zebrafish scale image processing, Erk activity and tissue flow quantification sample MATLAB code is available at <https://github.com/Desimonea/DeSimoneErkwaves2020>.

28. Lee, Y., Grill, S., Sanchez, A., Murphy-Ryan, M. & Poss, K. D. Fgf signaling instructs position-dependent growth rate during zebrafish fin regeneration. *Development* **132**, 5173–5183 (2005).
29. Nachtrab, G., Kikuchi, K., Tornini, V. A. & Poss, K. D. Transcriptional components of anteroposterior positional information during zebrafish fin regeneration. *Development* **140**, 3754–3764 (2013).
30. McKinney, S. A., Murphy, C. S., Hazelwood, K. L., Davidson, M. W. & Looger, L. L. A bright and photostable photoconvertible fluorescent protein. *Nat. Methods* **6**, 131–133 (2009).
31. Wan, J., Ramachandran, R. & Goldman, D. HB-EGF is necessary and sufficient for Müller glia dedifferentiation and retina regeneration. *Dev. Cell* **22**, 334–347 (2012).
32. Wan, J., Zhao, X. F., Vojtek, A. & Goldman, D. Retinal injury, growth factors, and cytokines converge on β -catenin and pStat3 signaling to stimulate retina regeneration. *Cell Rep.* **9**, 285–297 (2014).
33. Trapnell, C., Pachter, L. & Salzberg, S. L. TopHat: discovering splice junctions with RNA-seq. *Bioinformatics* **25**, 1105–1111 (2009).
34. Liao, Y., Smyth, G. K. & Shi, W. featureCounts: an efficient general purpose program for assigning sequence reads to genomic features. *Bioinformatics* **30**, 923–930 (2014).
35. Love, M. I., Huber, W. & Anders, S. Moderated estimation of fold change and dispersion for RNA-seq data with DESeq2. *Genome Biol.* **15**, 550 (2014).
36. Subramanian, A. et al. Gene set enrichment analysis: a knowledge-based approach for interpreting genome-wide expression profiles. *Proc. Natl Acad. Sci. USA* **102**, 15545–15550 (2005).
37. Mootha, V. K. et al. Integrated analysis of protein composition, tissue diversity, and gene regulation in mouse mitochondria. *Cell* **115**, 629–640 (2003).
38. Thompson, J. D. et al. Identification and requirements of enhancers that direct gene expression during zebrafish fin regeneration. *Development* **147**, dev191262 (2020).
39. Molina, G. et al. Zebrafish chemical screening reveals an inhibitor of Dusp6 that expands cardiac cell lineages. *Nat. Chem. Biol.* **5**, 680–687 (2009).
40. Carroll, K. J. et al. Estrogen defines the dorsal–ventral limit of VEGF regulation to specify the location of the hemogenic endothelial niche. *Dev. Cell* **29**, 437–453 (2014).
41. Luu-The, V., Paquet, N., Calvo, E. & Cumps, J. Improved real-time RT-PCR method for high-throughput measurements using second derivative calculation and double correction. *Biotechniques* **38**, 287–293 (2005).
42. Amat, F. et al. Fast, accurate reconstruction of cell lineages from large-scale fluorescence microscopy data. *Nat. Methods* **11**, 951–958 (2014).
43. Sommer, C., Straehle, C., Kothe, U. & Hamprecht, F. A. ilastik: interactive learning and segmentation toolkit. In 2011 IEEE Symposium on Biomedical Imaging: From Nano to Macro, 230–233 (IEEE, 2011).
44. Grossmann, C., Roos, H.-G. r. & Stynes, M. *Numerical Treatment of Partial Differential Equations* (Springer, 2007).

Acknowledgements We thank J. Burris, S. Miller, K. Oliveri, C. Dolan, L. Frauen and D. Stutts for zebrafish care; J. M. Cook and the Duke Cancer Institute Flow Cytometry Facility for help with flow cytometry; A. Kawakami and B. Riley for sharing transgenic fish; I. Rask, H. Kim, S. Li and Z. Weishampel for help with data curation, imaging, fish husbandry and genotyping; V. Cigliola for advice regarding gene expression experiments; M. Bagnat, A. Puliafito, B. Shraiman, S. Streichen and M. Vergassola for scientific discussions and advice; and P. Gönczy, B. Hogan and B. Mathey-Prevot for critical reading of the manuscript. A.D. was supported by Early (P2ELP3_172293) and Advanced (P300PA_177838) Postdoc. Mobility fellowships from the Swiss National Science Foundation. B.D.C. and V.A.T. were supported by NSF Graduate Research Fellowships (1106401). This work was supported by an Innovation in Stem Cell Science Award from the Shipley Foundation, Inc. to S.D. and N.I.H. grant (R01-AR076342) to K.D.P. and S.D.

Article

Author contributions A.D., K.D.P. and S.D. conceived the project and designed the experiments; A.D., M.N.E., B.D.C. and J.W. conducted experiments; A.D., B.D.C., V.A.T. and A.C. generated transgenic fish; A.D. and B.D.C. developed the imaging platform; A.D. developed computational tools and performed data analysis with help from L.H. and J.O.; A.D., L.H. and S.D. developed the theory and wrote simulation codes; A.D. and L.H. performed and analysed the simulations; A.D., K.D.P. and S.D. wrote the paper with comments from all authors.

Competing interests The authors declare no competing interests.

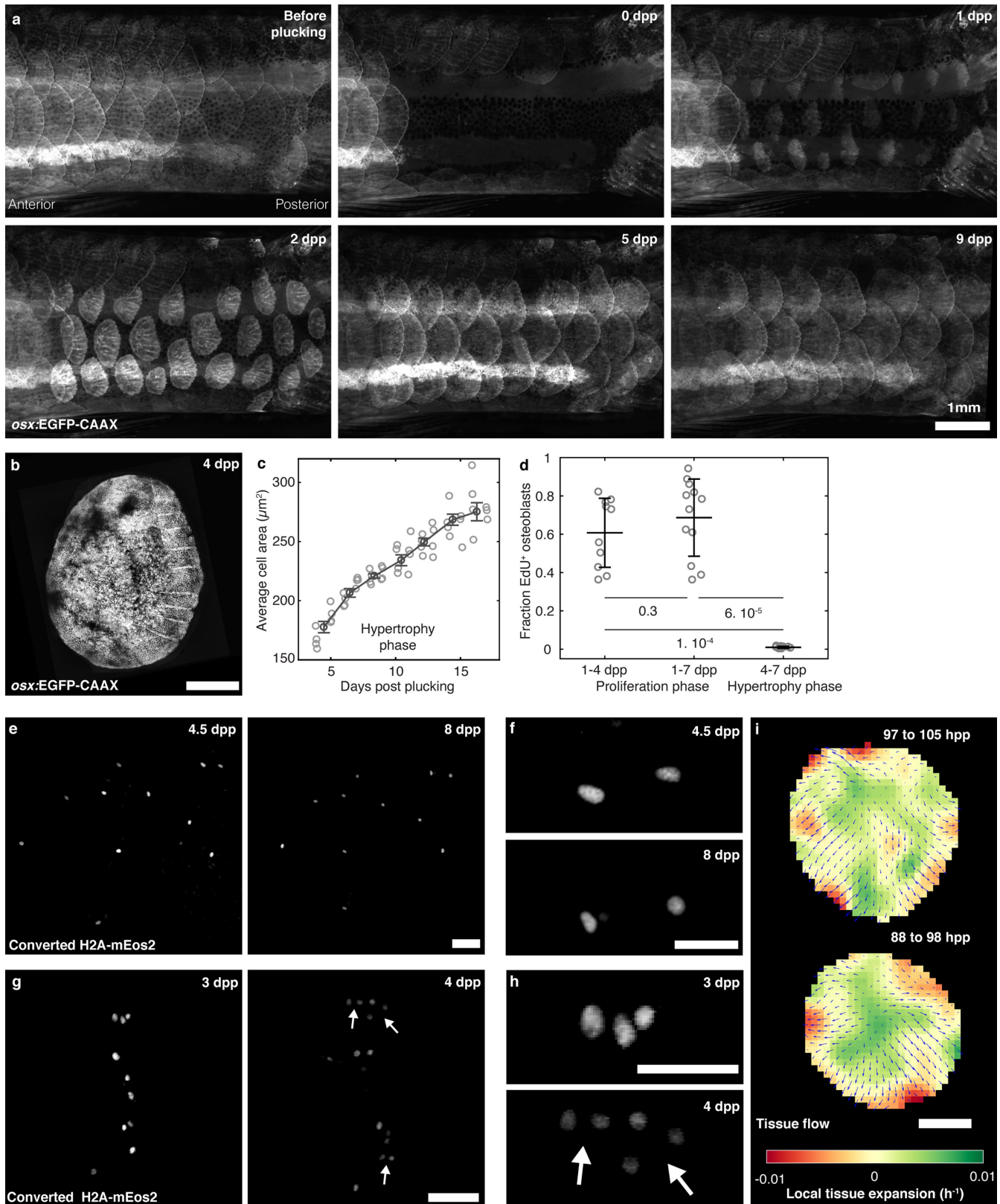
Additional information

Supplementary information is available for this paper at <https://doi.org/10.1038/s41586-020-03085-8>.

Correspondence and requests for materials should be addressed to K.D.P. or S.D.T.

Peer review information *Nature* thanks Michiyuki Matsuda, Patrick Mueller, David Parichy and the other, anonymous, reviewer(s) for their contribution to the peer review of this work.

Reprints and permissions information is available at <http://www.nature.com/reprints>.

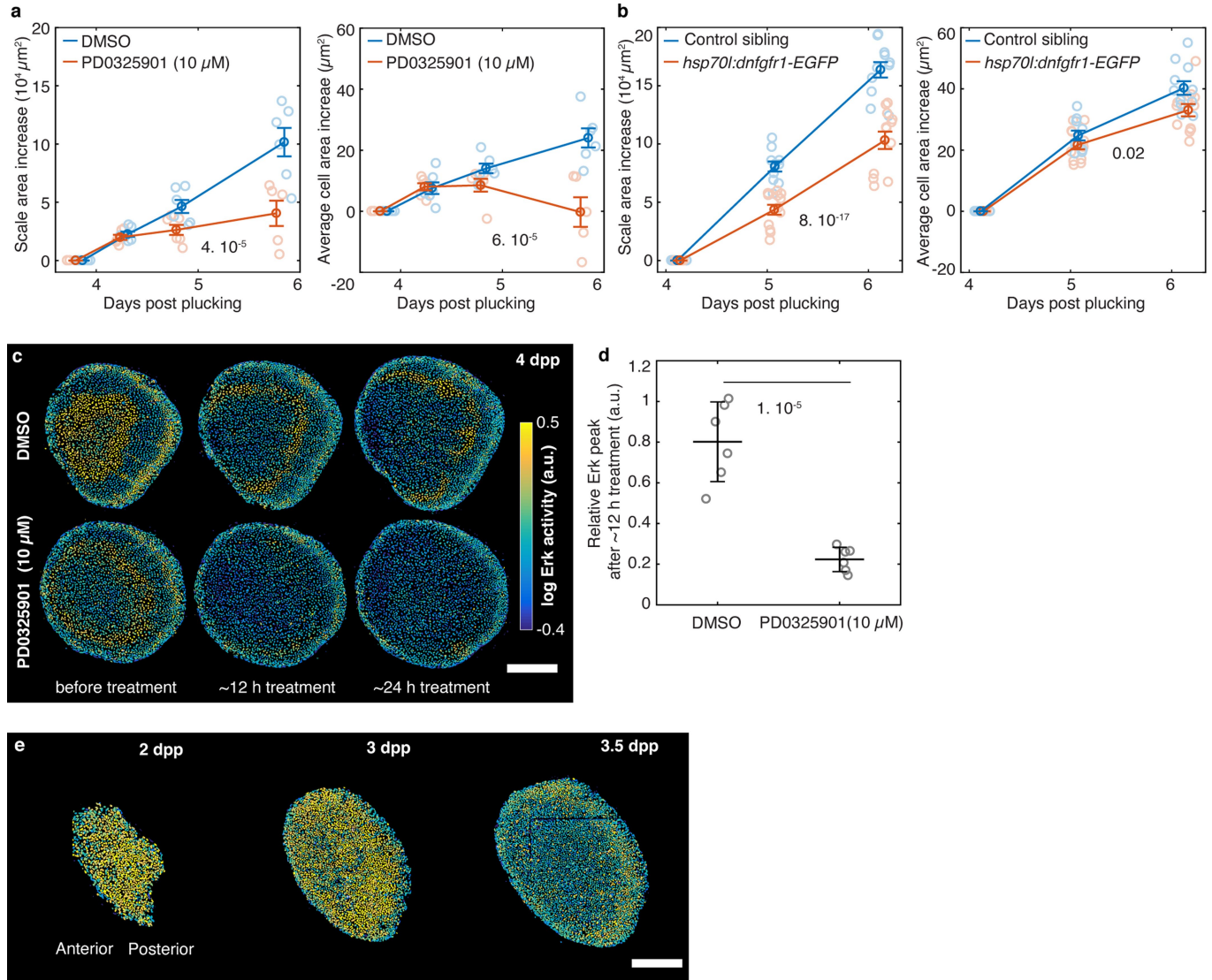


Extended Data Fig. 1 | See next page for caption.

Article

Extended Data Fig. 1 | Scale regeneration in zebrafish. This figure contains data indicating that osteoblasts display minimal proliferation after 4 dpp and that their hypertrophic growth is patterned. **a**, Array of regenerating scales on the trunk of a fish. $n > 50$ fish from > 5 independent experiments. **b**, Osteoblasts form a continuous monolayer in zebrafish scales (Supplementary Video 2). $n > 50$ fish from > 5 independent experiments. Scale bar, 250 μm . **c**, Average cell area (error bars, mean with s.e.m.; $n = 4$ scales in 4 fish in a single trial) in scale regeneration. **d**, Fraction of EdU-positive nuclei during the proliferative and hypertrophic phases. Error bars, mean with s.d.; each circle represents the fraction of positive nuclei among 500–2,000 nuclei from an individual scale; 1–4 dpp, $n = 4$ fish; 1–7 dpp, $n = 2$ fish; 4–7 dpp, $n = 4$ fish; single trial; two-sided Wilcoxon's rank-sum test P is indicated. Proliferative phase, fish are injected at 1 dpp and scales are collected at 4 dpp or 7 dpp, as indicated. Hypertrophic phase, fish are injected at 4.5 dpp and scales are collected at 7 dpp. **e**, Osteoblast nuclei tagged with the photoconvertible protein mEos2 are photoconverted during the hypertrophic phase (4.5 dpp), imaged daily and

tracked thereafter. No nuclei were observed to divide, and almost all could still be detected after 4 days. $n = 55/58$ cells from 5 fish tracked from 4.5 to 8 dpp pooled from 2 independent experiments. Probability of cell division is less than 2% per day at 95% confidence. Scale bar, 50 μm . **f**, High magnification of **e**. Scale bar, 25 μm . **g**, Osteoblast nuclei tagged with the photoconvertible protein mEos2 are photoconverted during the proliferative phase (3 dpp) and imaged the day after. Cell division can be detected: 9 divisions, scored by the increase of converted nuclei, from 3 to 4 dpp in 55 converted cells from 5 scales from 2 fish (single trial); compatible with a total proliferation rate of 0.156 ± 0.003 per cell per day for the entire scale; white arrows indicates likely division events. Scale bar, 50 μm . **h**, High magnification of **g**. Scale bar, 25 μm . **i**, Examples of tissue velocity field \bar{v} (tissue flow, blue arrows) and its divergence $\nabla \cdot \bar{v}$ (heat map), indicating the pattern of tissue expansion and contraction. $n > 10$ fish from 5 independent experiments. Tissue flows are calculated tracking individual cell movements for about 9 h (one frame every 3 h). Scale bar, 250 μm .

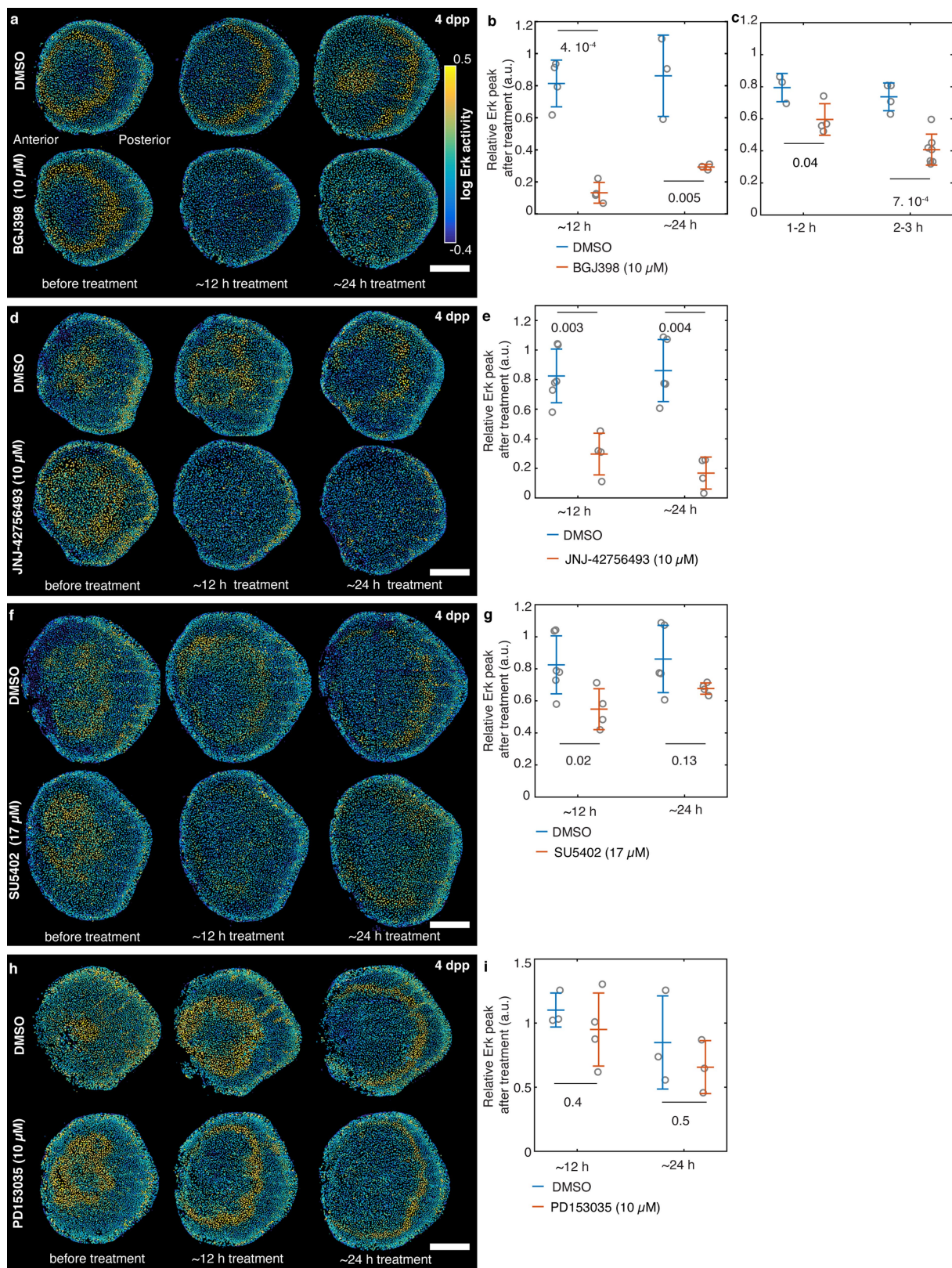


Extended Data Fig. 2 | Manipulation of Erk signalling during scale regeneration; Erk activity at 2–3 dpp.

a, Scale area increase (left) and average cell area increase (right) in fish treated with the Mek inhibitor PD0325901 and DMSO control (with s.e.m.; $n=6$ scales from 6 fish in each condition pooled from 2 independent experiments; chi-squared test P is indicated). **b**, Scale area increase (left) and average cell area increase (right) as function of time in fish expressing a gene encoding a dominant negative version of the fibroblast growth factor receptor 1 (Fgfr1) downstream of the heat-shock promoter *hsp70l* (*hsp70l:dngfr1-eGFP*) and control siblings not carrying the transgene. Fish are heat-shocked every day, starting before the first time point at 4 dpp

(with s.e.m.; $n=12$ scales from 3 fish per condition in a single trial; chi-squared test P is indicated). **c, d**, Example (c) and quantification (d) of Erk activity in fish treated with the Mek inhibitor PD0325901 and DMSO control. Error bars, mean with s.d.; each circle represents a scale from an individual fish, pooled from 2 independent experiments; unpaired two-sided log-normal test P is indicated. **e**, Example of Erk activity in a regenerating scale at 2 and 3 dpp. Erk activity is activated in a uniform pattern at 2 dpp. $n=5$ scales from 5 fish in a single trial. At around 3 dpp, Erk switches off starting from the scale centre. $n=6$ scales from 5 fish in a single trial. Scale bars, 250 μm .

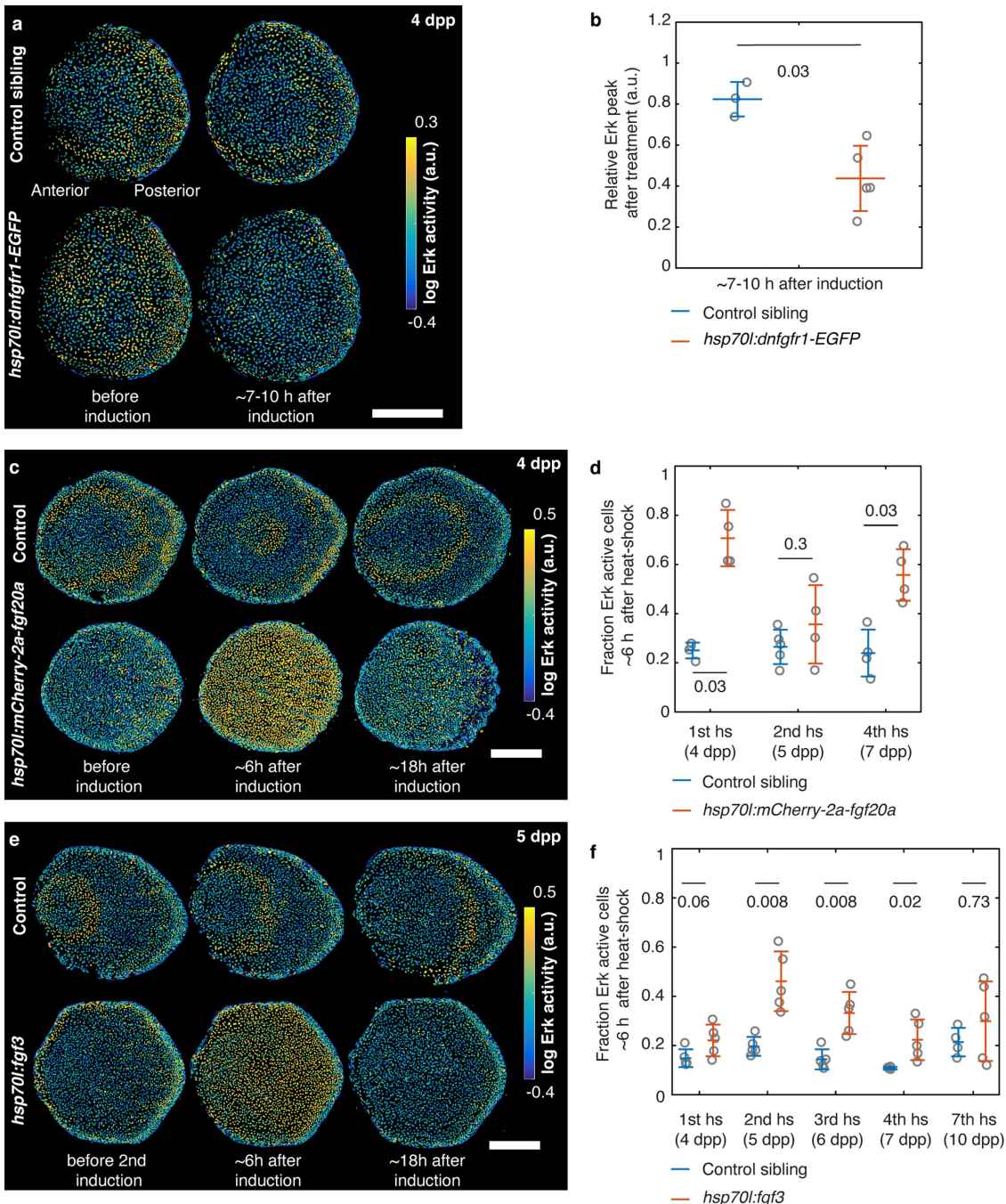
Article



Extended Data Fig. 3 | See next page for caption.

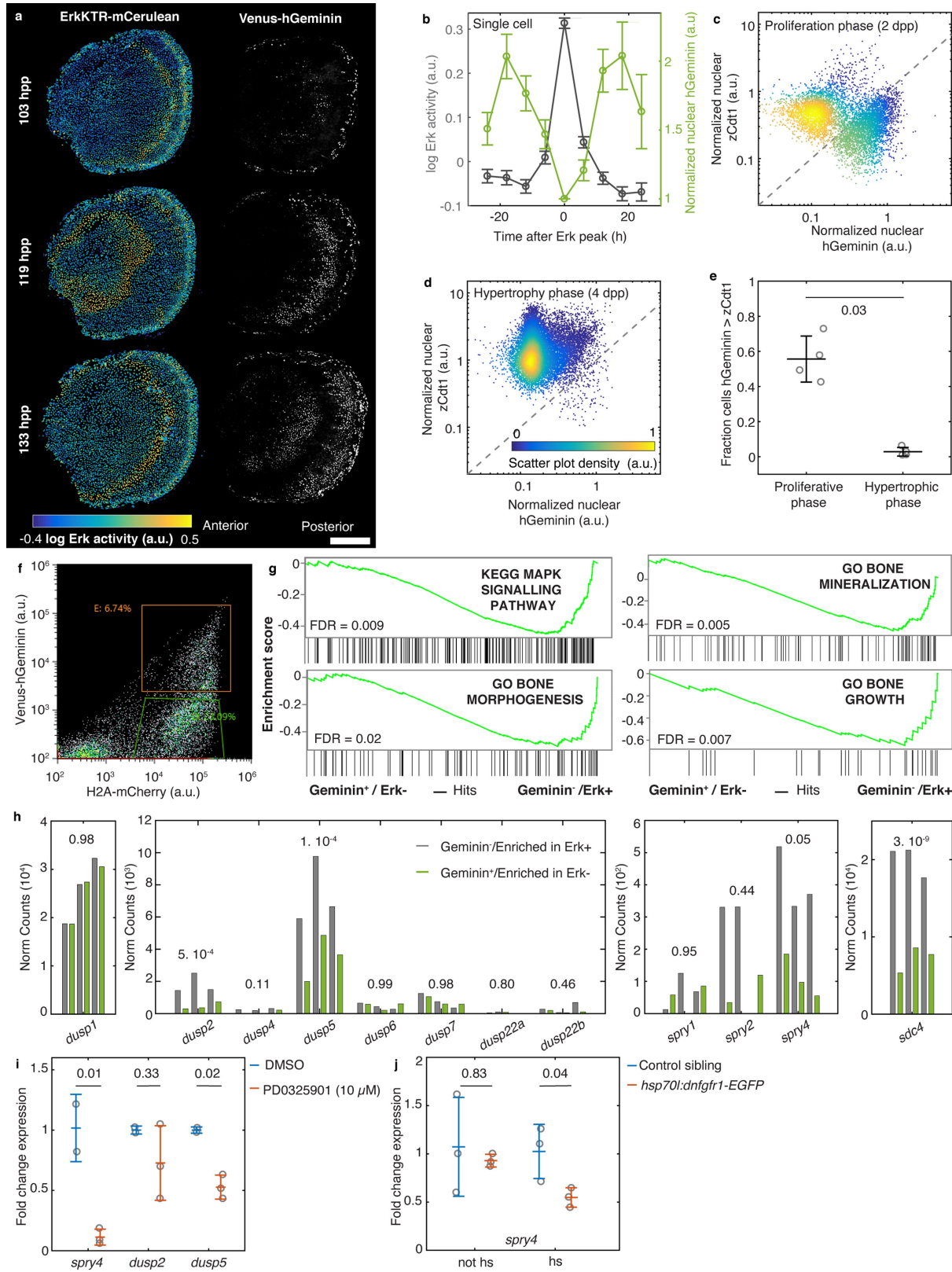
Extended Data Fig. 3 | Pharmacological inhibition of Fgfr and Egfr signalling during scale regeneration. **a, b**, Example (**a**) and quantification (**b**) of Erk activity in fish treated with the pan-Fgfr inhibitor BGJ398 and DMSO control. Error bars, mean with s.d.; $n=4$ scales from 4 fish per condition; data from a single trial, replicated in 2 additional independent experiments; unpaired two-sided log-normal test P is indicated. **c**, Quantification of Erk activity in fish treated with the pan-Fgfr inhibitor BGJ398 for 1–3 h and DMSO control. Error bars, mean with s.d.; DMSO, $n=4$ scales from 4 fish pooled from two independent experiments, BGJ398, $n=7$ scales from 7 fish pooled from 3 independent experiments; unpaired two-sided log-normal test P is indicated. **d, e**, Example (**d**) and quantification (**e**) of Erk activity in fish treated with the pan-Fgfr inhibitor JNJ-42756493 and DMSO control. Error bars, mean with s.d.;

DMSO, $n=6$ scales from 6 fish in a single trial; JNJ-42756493, $n=4$ scales from 4 fish in a single trial; unpaired two-sided log-normal test P is indicated. **f, g**, Example (**f**) and quantification (**g**) of Erk activity in fish treated with the Fgfr inhibitor SU5402 and DMSO control. Error bars, mean with s.d.; DMSO, $n=6$ scales from 6 fish in a single trial; SU5402, $n=4$ scales from 4 fish in a single trial; unpaired two-sided log-normal test P is indicated. Control fish are the same as in **d, e, h, i**. Example (**h**) and quantification (**i**) of Erk activity in fish treated with the Egfr inhibitor PD153035 and DMSO control. Error bars, mean with s.d.; DMSO, $n=3$ scales from 3 fish in a single trial; PD153035, $n=4$ scales from 4 fish per condition in a single trial; unpaired two-sided log-normal test P is indicated. Scale bars, 250 μm .



Extended Data Fig. 4 | Expression of *dnfgfr1* and overexpression of *fgf3* and *fgf20a* during scale regeneration. **a, b,** Example (a) and quantification (b) of Erk activity in fish expressing a gene encoding a dominant negative version of the fibroblast growth factor receptor 1 (Fgfr1) downstream of the heat-shock promoter *hsp70l* (*hsp70l:dnfgfr1-eGFP*) and control siblings not carrying the transgene. Error bars, mean with s.d.; control, $n=3$ scales from 2 fish in a single trial; *dnfgfr1*, 5 scales from 3 fish in a single trial; unpaired two-sided log-normal test P is indicated. In 1/5 scales in *hsp70l:dnfgfr1-eGFP* fish, we observed that a new wave originated at 108 hpp. Erk peak activity after 24 h treatment could not be measured as waves reached the scale border. **c, d,** Example (c) and quantification (d) of Erk activity in fish overexpressing *fgf20a* downstream of the heat-shock promoter *hsp70l* (*hsp70l:mCherry-2a-fgf20a*) and in control siblings. Error bars, mean with s.d.; 4 and 7 dpp, $n=4$ scales from 4 fish per

condition in a single trial; 5 dpp control, $n=5$ scales from 4 fish pooled from 2 independent experiments, *hsp70l:mCherry-2a-fgf20a*, $n=4$ scales from 4 fish pooled from 2 independent experiments; two-sided Wilcoxon's rank-sum test P is indicated. Heat-shock was performed everyday starting from 4 dpp, and Erk activity was measured thereafter (approximately 6 h after the start of the heat-shock) (Extended Data Fig. 8a, b). **e, f,** Example (e) and quantification (f) of Erk activity in fish overexpressing *fgf3* downstream of the heat-shock promoter *hsp70l* (*hsp70l:fgf3*) and in control siblings. Error bars, mean with s.d.; $n=5$ scales from 5 fish per condition in a single trial; two-sided Wilcoxon's rank-sum test P is indicated. Heat-shock was performed everyday starting from 4 dpp, and Erk activity was measured thereafter (approximately 6 h after the start of the heat-shock) (Extended Data Fig. 9a, b). Scale bars, 250 μ m.



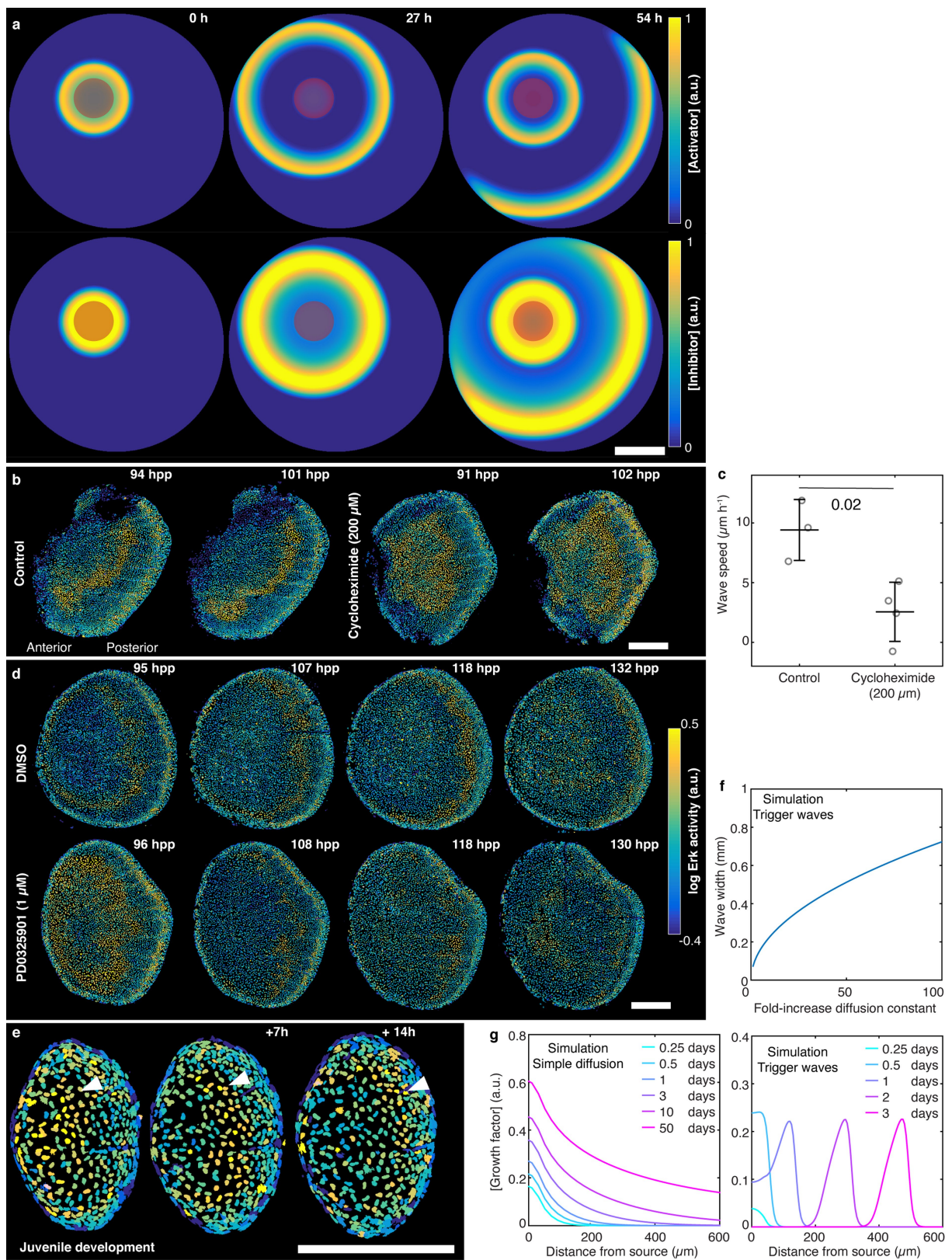
Extended Data Fig. 5 | See next page for caption.

Article

Extended Data Fig. 5 | Sequencing strategy for osteoblasts indicates increased transcript abundance of Erk inhibitors in Erk active cells.

a, Erk activity and *osx*:Venus–hGeminin signal in regenerating scales at different time-points are shown. $n > 10$ fish from >5 independent experiments. **b**, Venus–hGeminin signal as a function of time from Erk peak. Error bars, mean with s.e.m.; $n = 89$ cells from 3 scales from 3 fish in a single trial; for each cell track, $t = 0$ is the time of the Erk peak; Erk data are the same as presented in Fig. 2f. hGeminin nuclear signal is normalized to cytoplasmic signal. **c, d**, *osx*:hGeminin signal and *osx*:mCherry–zCdt1 signal (normalized for the respective cytoplasmic signals) in individual cells of a representative scale ($n = 4$ scales from 4 fish from a single experiment, replicated in 2 additional independent experiments; quantified in e) during the proliferative (c) and hypertrophy phases (d). **e**, Fraction of osteoblasts in proliferative state (normalized Venus–hGeminin > normalized mCherry–zCdt1) during the proliferative and hypertrophic phases of scale regeneration. Error bars, mean with s.d.; each circle is a scale from an individual fish in a single trial; two-sided Wilcoxon's rank-sum test is indicated. **f**, Flow-cytometry strategy to sort two populations of osteoblasts (H2A–mCherry $^+$): one enriched for Venus–hGeminin $^-$ Erk active cells (Erk $^-$) ($D, 9 \times 10^4, 8 \times 10^4$ and 5×10^4 cells in the three samples) and one enriched for Venus–hGeminin $^+$ Erk $^+$ inactive cells (Erk $^+$) ($E, 4 \times 10^4, 5 \times 10^4, 2 \times 10^4$ cells in the three samples). **g**, Gene set enrichment

analysis for the Kyoto Encyclopedia of Genes and Genomes MAPK signalling pathway, Gene Ontology bone mineralization, morphogenesis and growth. FDR, false discovery rate. Data from 3 samples pooled from 2 independent experiments. **h**, Normalized counts for expressed Erk-related *dusp* genes (*dusp1*, *dusp2*, *dusp4*, *dusp5*, *dusp6*, *dusp7*, *dusp22a* and *dusp22b*), sprouty (*spry1*, *spry2* and *spry4*) genes and the transmembrane proteoglycan *syndecan 4* (*sdc4*). DeSeq2 P -adjusted is indicated. **i**, Fold change of Erk inhibitory gene transcripts in regenerating scales of fish treated with the Mek inhibitor PD0325901 with respect to DMSO controls. Error bars, mean with s.d.; unpaired two-sided log-normal test P is indicated; 4 dpp scales are used; DMSO, $n = 2$ samples in a single trial; PD0325901, $n = 3$ samples in a single trial. **j**, Enrichment of Erk target *spry4* in scales of fish expressing a gene encoding a dominant negative version of the fibroblast growth factor receptor 1 (Fgfr1) downstream of the heat-shock promoter *hsp70l* (*hsp70l:dnfgfr1-eGFP*) with respect to control siblings. Error bars, mean with s.d.; unpaired two-sided log-normal test P is indicated; 4 dpp scales are used; $n = 3$ samples per condition in a single trial. Heat-shocked (hs) *hsp70l:dnfgfr1-eGFP* fish are compared with heat-shocked siblings not carrying the transgene. As an additional control, not heat-shocked (not hs) *hsp70l:dnfgfr1-eGFP* fish are compared with not heat-shocked siblings not carrying the transgene. Scale bar, 250 μ m.

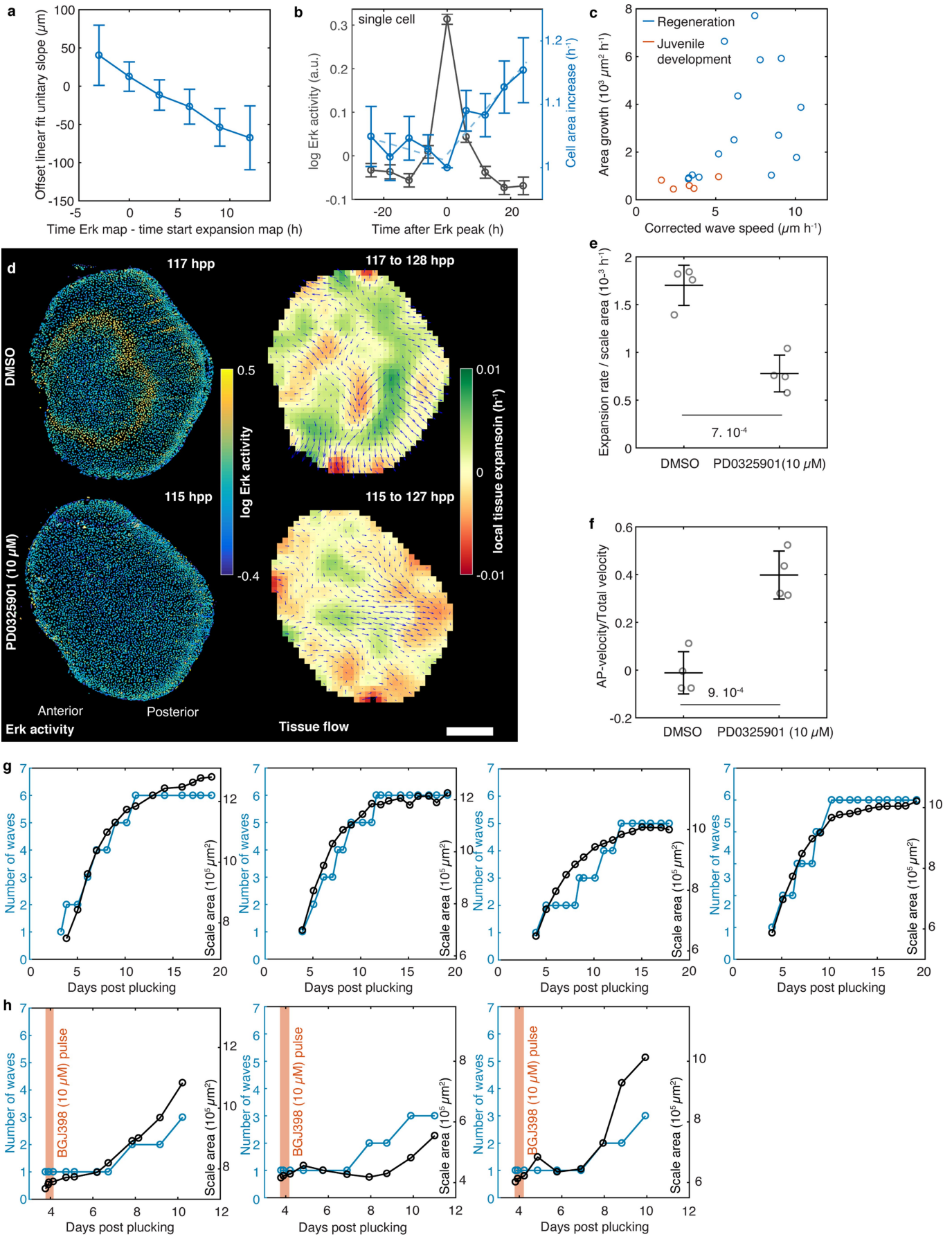


Extended Data Fig. 6 | See next page for caption.

Article

Extended Data Fig. 6 | Tests and consequences of trigger wave model. This figure contains extended details on the mathematical model of Erk waves, on the predictions of the models and their experimental tests. **a**, Mathematical model of Erk dynamics including a diffusible activator, such as Fgf, in turn activated by Erk, and a delayed inhibitor. Activator and inhibitor concentrations (heat map) as a function of time are shown. Red dashed region, activator source region. **b, c**, Examples of Erk activity and quantifications of wave speed (corrected for tissue growth) in regenerating scales in fish treated with cycloheximide at 4 dpp and controls. Error bars, mean with s.d.; each circle represents a scale from an individual fish; single trial. **d**, Example of Erk activity in fish treated with a concentration of the Mek inhibitor PD0325901 that slows

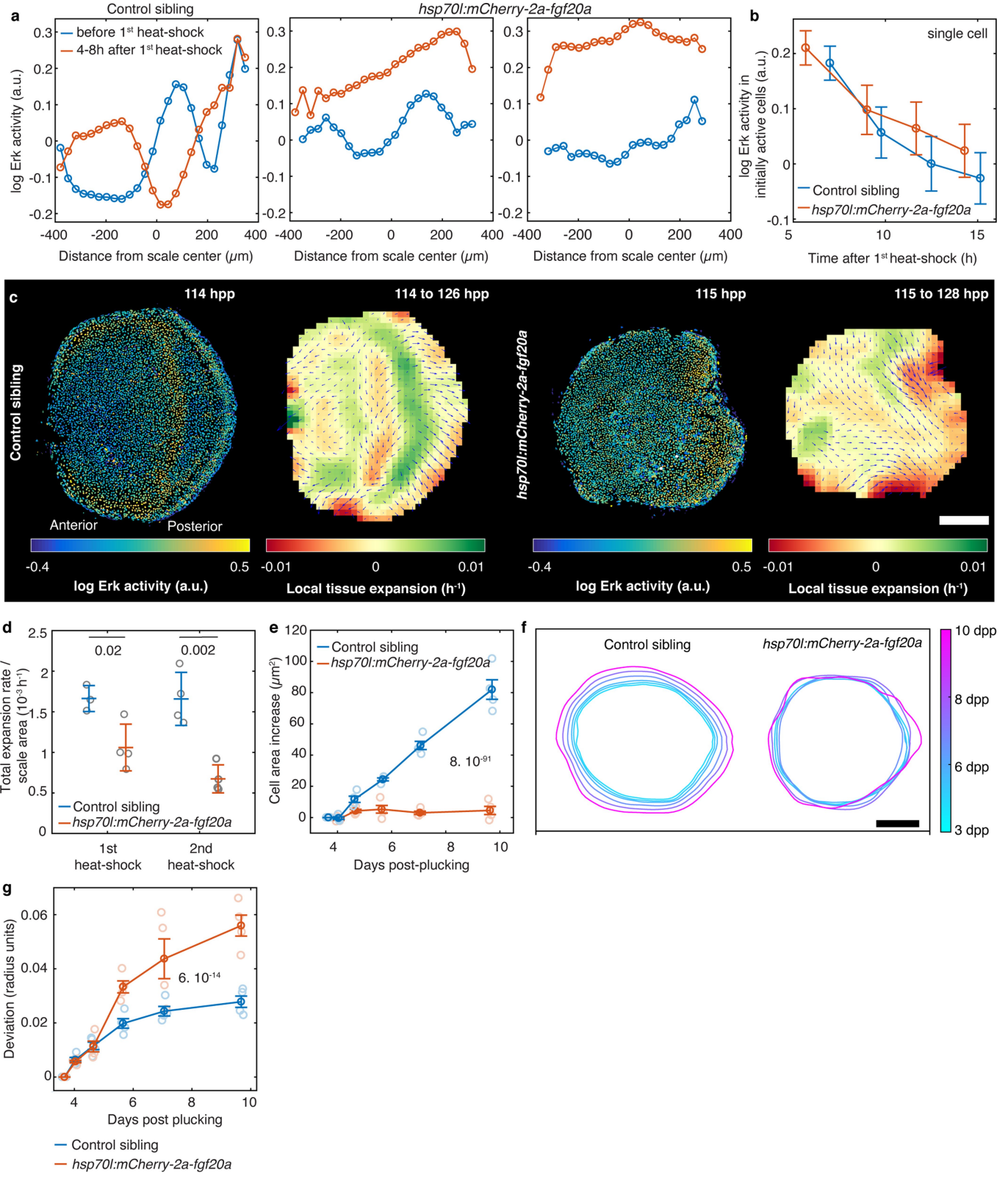
wave propagation but does not completely impair it, and DMSO control (see Fig. 3f for Erk wave speed quantification, $n=7$ scales from 7 fish pooled from 3 independent experiments). **e**, Example of Erk activity, organized in an expanding ring (arrowheads), in a developing scale in a juvenile fish throughout time. $n>15$ scales in 4 fish in a single trial. **f**, Wave width for different fold-increases of the activator diffusion constant (simulation; with respect to the standard simulation of Fig. 3, Methods). **g**, Simulation of growth factor concentration as a function of time in a simple diffusion model and in the Erk trigger wave model. In both models, D is approximately $0.1\mu\text{m}^2\text{s}^{-1}$ (Methods). Scale bars, $250\mu\text{m}$.



Extended Data Fig. 7 | See next page for caption.

Article

Extended Data Fig. 7 | Erk activity is required for tissue expansion during zebrafish scale hypertrophy. **a**, Time delay of expansion peak position versus Erk peak position. Time delay is measured fitting the relationship between expansion peak position and Erk peak position for different lag times with a linear fit (unitary slope; error bars, best fit with 95% confidence interval; $n=18$ expansion peaks from 16 scales from 12 fish pooled from >5 independent experiments). The expansion peak is taken at the start of the 9-h-long time-window considered to calculate flows. For clarity, a positive lag time means that the position of the Erk peak is taken at a time subsequent to the initial point of the time window used to calculate the expansion peak. **b**, Average single-cell area increase as a function of time from Erk peak. Error bars, mean with s.e.m.; $n=89$ cells from 3 scales from 3 fish in a single trial; for each cell track, $t=0$ is the time of the Erk peak; Erk data are the same presented in Fig. 2f. Each cell area is normalized to cell area at the time of Erk peak (cell area was measured manually using the Erk KTR-mCerulean signal). Dashed lines, linear fit of normalized cell areas before and after the Erk peak. Slope before peak: $(-0.002 \pm 0.002) \text{ h}^{-1}$; slope after peak: $(0.006 \pm 0.002) \text{ h}^{-1}$; with 68% confidence interval. **c**, Scale area growth as a function of Erk wave speed, corrected for tissue growth, in ontogenetic and regenerating scales. Circles represent individual scales from 12 (regeneration, pooled from >5 independent experiments) and 3 (juvenile development, single trial) fish; Spearman's correlation coefficient 0.75, $P=2 \times 10^{-4}$. **d**, Erk activity, tissue velocity field \bar{v} (tissue flow, blue arrows) and its divergence $\nabla \cdot \bar{v}$ (heat map) in scales in fish treated with the Mek inhibitor PD0325901 and DMSO control. $n=4$ scales from 4 fish per condition pooled from 2 independent experiments. In **d–f**, fish are treated at 4 dpp and imaged about 24 h later for about 12 h at 3-h frame rate. **e, f**, Total expansion rate of expanding regions (**e**), normalized for scale area, and anterior–posterior (AP)-velocity component (**f**) in fish treated with PD0325901 (10 μM) and DMSO control. Error bars, mean with s.d.; $n=4$ scales from 4 fish per condition pooled from 2 independent experiments; unpaired two-sided Student's *t*-test is shown. Fish are treated at 4 dpp and imaged about 24 h later for around 12 h (1 frame every 3 h). **g**, Cumulative number of waves and scale area as a function of time throughout entire scale regeneration (single trial). **h**, Cumulative number of waves and scale area as a function of time in scales treated with the pan-Fgfr inhibitor BGJ398 (10 μM) for around 3 h at 4 dpp (orange area) and transferred to fresh water thereafter. Two pooled independent experiments. Scale bar, 250 μm .

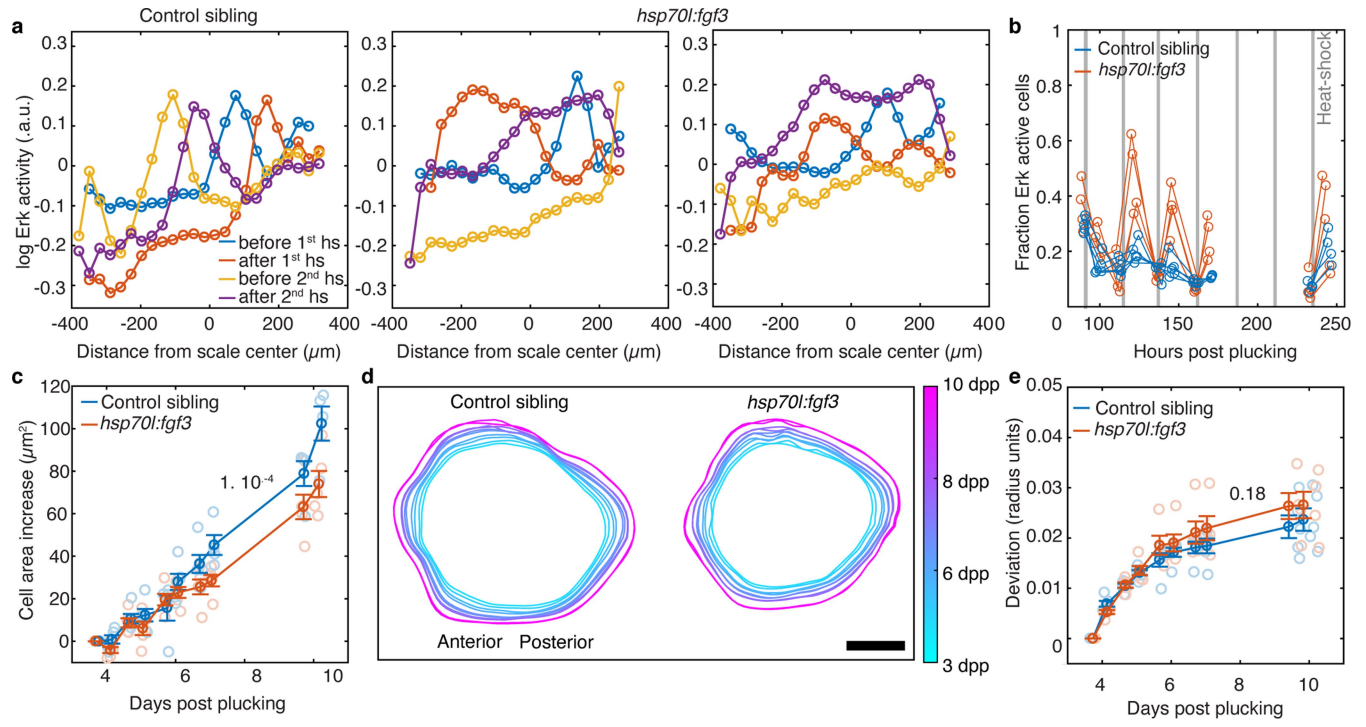


Extended Data Fig. 8 | See next page for caption.

Article

Extended Data Fig. 8 | Effects of ectopic and tissue-wide Fgf20a pulses on scale regeneration. This figure indicates that tissue-wide and synchronous Erk oscillations induced by Fgf20a ectopic expression display similar temporal dynamics to baseline, wave-dependent Erk activation, and that they impair tissue growth. **a**, Quantification of spatial pattern of Erk activity in 4-dpp regenerating scales in fish expressing *fgf20a* downstream of the heat-shock promoter *hsp70l* (*hsp70l:mCherry-2a:fgf20a*) and control siblings not carrying the transgene. Erk activity is averaged along a 240 μm -wide stripe passing through the scale centre and the wave origin. $n = 4$ scales from 4 fish per condition, data from a single trial, replicated in 2 additional independent experiments. **b**, Erk activity in initially active cells (cytoplasmic Erk KTR > 1.1 nuclear Erk KTR) in *hsp70l:mCherry-2a:fgf20a* fish and control siblings not carrying the transgene. Error bars, mean with s.e.m.; $n = 3$ scales from 3 fish per condition pooled from 2 independent experiments. Transgenic *fgf20a* expression was induced by heat-shock at 3.5 dpp. Scales were imaged starting 4 h after the start of heat-shock for around 12 h (1 frame every 3 h). **c**, Erk activity, tissue velocity field \bar{v} (tissue flow, blue arrows) and its divergence $\nabla \cdot \bar{v}$ (heat map) indicating tissue expansion, in regenerating scales in *hsp70l:mCherry-2a:fgf20a* fish and control siblings not carrying the transgene. Transgenic *fgf20a* expression was induced by heat-shock at 3.5 and at 4.5 dpp. Scales were imaged starting 4 h after heat-shock for around 12 h (1 frame every 3 h). Quantifications in **d**. **d**, Tissue expansion in regenerating scales in *hsp70l:mCherry-2a:fgf20a*

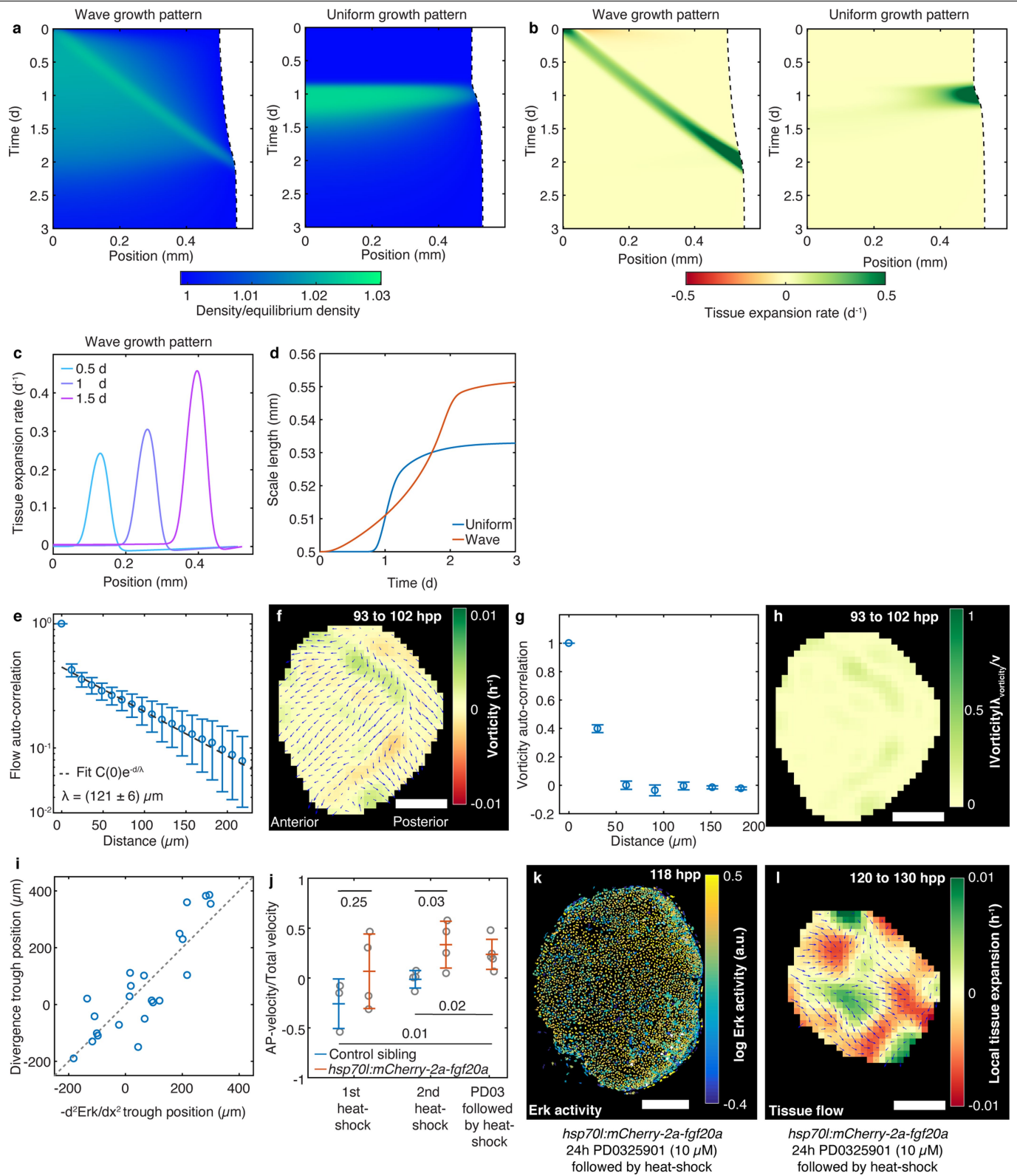
fish and control siblings not carrying the transgene. Error bars, mean with s.d.; each circle represents a scale from an individual fish, except for 'Control sibling' in '2nd heat-shock' in which $n = 4$ scales from 3 fish are shown; pooled from 2 independent experiments; unpaired two-sided Student's *t*-test *P* is indicated. Transgenic *fgf20a* expression was induced by heat-shock at 3.5 and at 4.5 dpp. Scales were imaged starting 4 h after heat-shock for about 9 h (first heat-shock) or about 12 h (second heat-shock) (1 frame every 3 h). **e**, Average cell area increase as function of time in regenerating scales in *hsp70l:mCherry-2a:fgf20a* fish and control siblings not carrying the transgene. Error bars, mean with s.e.m.; $n = 4$ scales from 4 fish per condition in a single trial; chi-squared test *P* is indicated. Transgenic *fgf20a* expression is induced by heat-shocking fish every day at the same time (Methods), starting after the first time point. **f,g**, Example of scale morphology as a function of time in fish expressing *hsp70l:mCherry-2a:fgf20a* and control siblings not carrying the transgene. $n = 4$ scales from 4 fish per condition in a single trial (**f**). Average deviation of scale morphology (**g**) (error bars, mean with s.e.m., $n = 4$ scales from 4 fish per condition in a single trial) is measured with respect to before heat-shock by calculating the total discrepancy of the rescaled scale borders in polar coordinates (Methods). Chi-squared test *P* is indicated. Transgenic *fgf20a* expression is induced by heat-shocking fish every day at the same time (Methods), starting after the first time point. Scale bar, 250 μm .



Extended Data Fig. 9 | Effects of ectopic and tissue-wide Fgf3 pulses on scale regeneration. This figure indicates that Fgf3-induced tissue-wide and synchronous Erk oscillations lead to impaired tissue growth. **a, b**, Quantification of spatial (a) and temporal (b) patterns of Erk activity in regenerating scales in fish expressing *fgf3* downstream of the heat-shock promoter *hsp70l* (*hsp70l:fgf3*) and control siblings not carrying the transgene. $n = 5$ scales from 5 fish per condition from a single trial. Transgenic *fgf3* expression was induced by heat-shock every day; fish were imaged before and after heat-shock (shaded regions in b). In a, Erk activity is averaged along a 240 μm -wide stripe passing through the scale centre and the wave origin. In b, the fraction of active Erk cells with respect to total is calculated in the entire scale (cytoplasmic Erk KTR > 1.1 nuclear Erk KTR). **c**, Average cell area increase (with s.e.m.) as function of time in regenerating scales in *hsp70l:fgf3* fish and

control siblings not carrying the transgene. Error bars, mean with s.e.m.; $n = 5$ scales from 5 fish per condition in a single trial; chi-squared test P is indicated. Transgenic *fgf3* expression was induced by heat-shock every day starting from 3.5 dpp. Fish were imaged before and after heat-shock (shaded regions in b). **d, e**, Example of scale morphology as a function of time in fish expressing *hsp70l:fgf3* and control siblings not carrying the transgene. $n = 5$ scales from 5 fish per condition in a single trial (d). Average deviation of scale morphology (e) (error bars, mean with s.e.m., $n = 5$ scales from 5 fish per condition in a single trial) is measured with respect to before heat-shock by calculating the total discrepancy of the rescaled scale borders in polar coordinates (Methods). Chi-squared test P is indicated. Transgenic *fgf3* expression was induced by heat-shock every day; fish were imaged before and after heat-shock (shaded regions in b). Scale bar, 250 μm .

Article



Extended Data Fig. 10 | See next page for caption.

Extended Data Fig. 10 | Minimal mechanical model of tissue growth and tissue flow properties. **a–d**, Tissue density (**a**), tissue expansion rate (**b, c**) (calculated as $\frac{\partial v}{\partial x}$) and total tissue growth (**d**) in the case of wave-like and uniform basal tissue growth in 1D mathematical model of tissue growth (Supplementary Notes). **e**, Two-point correlator of tissue flow velocities in control scales. Error bars, mean with s.d.; $n=5$ scales from 5 fish pooled from 2 independent experiments. λ is the flow velocity correlation length (with 95% confidence interval). **f–h**, Vorticity of tissue velocity field (**f**), its two-point correlator (**g**) (error bars, mean with s.d.; $n=5$ scales from 5 fish pooled from 2 independent experiments) and adimensionalized vorticity (**h**) (v is the average flow absolute velocity and $\lambda_{\text{vorticity}}$ is the vorticity correlation length, estimated to be about 30 μm). $\lambda_{\text{vorticity}}$ is similar to the length used to calculate the vorticity itself, so it represents an upper limit; smaller values of $\lambda_{\text{vorticity}}$ would further decrease adimensionalized vorticity. Average absolute tissue flow vorticity for 5 scales from 5 fish pooled from 2 independent experiments: 0.0007 h^{-1} , 0.0009 h^{-1} , 0.0009 h^{-1} , 0.0008 h^{-1} and 0.0012 h^{-1} . Average tissue flow speed for 5 scales from 5 fish pooled from 2 independent experiments: 0.4 $\mu\text{m h}^{-1}$, 0.5 $\mu\text{m h}^{-1}$, 0.5 $\mu\text{m h}^{-1}$, 0.4 $\mu\text{m h}^{-1}$ and 0.5 $\mu\text{m h}^{-1}$. **i**, Position of the divergence trough, that is, compression peak (distance from scale centroid; calculated over 9 h), as a function of the position of the trough of $-\frac{d^2\text{Erk}}{dx^2}$ in which x is the distance from scale centroid. $n=16$ scales from 12 fish from >5 independent experiments; Pearson's correlation coefficient 0.87, $P=3 \times 10^{-8}$; dashed line: bisector of the axis. The divergence trough has intensity $(-0.002 \pm 0.002) \text{ h}^{-1}$ (s.d.; s.e.m. 0.0003 h^{-1}). **j**, Quantification of average AP

component of tissue flow velocity, normalized to the norm of the velocity vector, in regenerating scales in *hsp70l:mCherry-2a:fgf20a* fish and control siblings not carrying the transgene. Error bars, mean with s.d.; each circle represents a scale from an individual fish, except for 'Control sibling' in '2nd heat-shock' in which $n=4$ scales from 3 fish are shown and for 'PD03 followed by heat-shock' in which $n=5$ scales from 3 fish are shown; first and second heat-shock: pooled from 2 independent experiments each, PD03 followed by heat-shock: single trial; unpaired two-sided Student's *t*-test *P* is indicated. First heat-shock, transgenic *fgf20a* expression was induced by heat-shock at 3.5 dpp; second heat-shock, 3.5 and 4.5 dpp; PD03 followed by heat-shock, fish were treated with PD0325901 (10 μM) for 24 h at 4 dpp, then they were transferred to fresh water and heat-shocked. Finally, fish were returned to the chemical treatment and imaged. Scales were imaged starting 5 h after heat-shock for about 9 h (first heat-shock and PD03 followed by heat-shock) or 12 h (second heat-shock). **k**, Erk activity in scales treated with PD0325901 (10 μM) and then heat-shocked in fresh water, as described in **j**, but without returning them to chemical treatment, and imaged. Fraction of Erk active cells with respect to total from 4 scales from 2 fish in a single trial: 0.73, 0.75, 0.64, 0.45. **l**, Tissue velocity field \bar{v} (tissue flow, blue arrows) and its divergence $\nabla \cdot \bar{v}$ (heat map) indicating tissue expansion, in regenerating scales in *hsp70l:mCherry-2a:fgf20a* fish treated with PD0325901 (10 μM) for 24 h, then heat-shocked, returned to chemical treatment and imaged, as described in **j**. Quantifications are in **j** (single trial). Scale bars, 250 μm .

Corresponding author(s): Ken Poss and Stefano Di Talia

Last updated by author(s): 10 Nov, 2020

Reporting Summary

Nature Research wishes to improve the reproducibility of the work that we publish. This form provides structure for consistency and transparency in reporting. For further information on Nature Research policies, see [Authors & Referees](#) and the [Editorial Policy Checklist](#).

Statistics

For all statistical analyses, confirm that the following items are present in the figure legend, table legend, main text, or Methods section.

n/a Confirmed

- The exact sample size (n) for each experimental group/condition, given as a discrete number and unit of measurement
- A statement on whether measurements were taken from distinct samples or whether the same sample was measured repeatedly
- The statistical test(s) used AND whether they are one- or two-sided
Only common tests should be described solely by name; describe more complex techniques in the Methods section.
- A description of all covariates tested
- A description of any assumptions or corrections, such as tests of normality and adjustment for multiple comparisons
- A full description of the statistical parameters including central tendency (e.g. means) or other basic estimates (e.g. regression coefficient) AND variation (e.g. standard deviation) or associated estimates of uncertainty (e.g. confidence intervals)
- For null hypothesis testing, the test statistic (e.g. F , t , r) with confidence intervals, effect sizes, degrees of freedom and P value noted
Give P values as exact values whenever suitable.
- For Bayesian analysis, information on the choice of priors and Markov chain Monte Carlo settings
- For hierarchical and complex designs, identification of the appropriate level for tests and full reporting of outcomes
- Estimates of effect sizes (e.g. Cohen's d , Pearson's r), indicating how they were calculated

Our web collection on [statistics for biologists](#) contains articles on many of the points above.

Software and code

Policy information about [availability of computer code](#)

Data collection

Confocal imaging data was collected on a Leica SP8 microscope using LAS X 2.0.1.14392 software. A Zeiss AxioZoom V16 and Zen Pro 2012 software was used to acquire illustrative low magnification images. Quantitative PCR was performed on a Roche LightCycler 480 with Software release 1.5.0 SP4.

Data analysis

Image processing and imaging data analysis were performed with custom-written MATLAB (Mathworks; version R2016b) software. For osteoblast counting and Erk activity quantification, nuclei were segmented by TGGM software (Amat et al., 2014, *Nature Methods*). For tissue flow measurements, Ilastik 1.3.2, 1.3.3 software was used for nuclei segmentation and tracking (Sommer et al., 2011, *I S Biomed Imaging*). For gene expression analyses, reads were trimmed by Trim Galore (0.4.1, with -q 15 --paired) and then mapped with TopHat41 (v 2.1.1, with parameters --b2-very-sensitive --no-coverage-search and supplying the UCSC danRer10 refSeq annotation). Gene-level read counts were obtained using the featureCounts42 (v1.6.1) by the reads with MAPQ greater than 30. Bioconductor package DESeq243 (v 1.26.0) were employed for differential expression (DE) analysis. Gene Set Enrichment Analysis (GSEA) was used to define the enriched gene set for the pre-ranked homo sapiens homologs list by Wald statistics. Quantitative PCR was analysed on a Roche LightCycler 480 with Software release 1.5.0 SP4. Zebrafish scale image processing, Erk activity and tissue flow quantification sample MATLAB code is available at <https://github.com/desimonea/DeSimoneErkwaves2020>.

For manuscripts utilizing custom algorithms or software that are central to the research but not yet described in published literature, software must be made available to editors/reviewers. We strongly encourage code deposition in a community repository (e.g. GitHub). See the Nature Research [guidelines for submitting code & software](#) for further information.

Data

Policy information about [availability of data](#)

All manuscripts must include a [data availability statement](#). This statement should provide the following information, where applicable:

- Accession codes, unique identifiers, or web links for publicly available datasets
- A list of figures that have associated raw data
- A description of any restrictions on data availability

Reagents are available upon request. Transcriptomics data are available on Gene Expression Omnibus (GSE147551). The microscopy dataset consists of large files (>1 Tb); therefore, microscopy data are available from the authors, without limitation. Source data are provided with this paper.

Field-specific reporting

Please select the one below that is the best fit for your research. If you are not sure, read the appropriate sections before making your selection.

Life sciences Behavioural & social sciences Ecological, evolutionary & environmental sciences

For a reference copy of the document with all sections, see nature.com/documents/nr-reporting-summary-flat.pdf

Life sciences study design

All studies must disclose on these points even when the disclosure is negative.

Sample size	No statistical method was used to predetermine sample size. Sample sizes were chosen based on previous studies with similar methodologies: Brown et al., <i>Nature</i> , 2016; Tornini et al., <i>Curr Biol</i> , 2016; Cox et al., <i>Curr Biol</i> , 2018; Deneke et al., <i>Cell</i> , 2019.
Data exclusions	No samples were excluded from the analysis. At times, scale tissue or the neighboring tissue was visibly damaged. Scales that were recognized as damaged during imaging or data curation were not further imaged or processed.
Replication	All experiments were performed on multiple animals and data were pooled, as indicated in Legends. Experiments were replicated, as indicated in Legends. All attempts at replication were successful.
Randomization	Animals, mixed males and females, were randomly allocated in control and experimental groups. When possible, siblings were used for control and experimental groups.
Blinding	It was not possible to blind investigators during data collection, since animals in control and experimental groups can be distinguished by cell behaviors and/or fluorescent reporters. However, data quantification was performed automatically using the same computational algorithm. When necessary, human manual data curation was performed by blinded researchers, although often data from control and experimental groups can be recognized from phenotypes. Researchers were not blinded during data visualization.

Reporting for specific materials, systems and methods

We require information from authors about some types of materials, experimental systems and methods used in many studies. Here, indicate whether each material, system or method listed is relevant to your study. If you are not sure if a list item applies to your research, read the appropriate section before selecting a response.

Materials & experimental systems

n/a	Involved in the study
<input checked="" type="checkbox"/>	<input type="checkbox"/> Antibodies
<input checked="" type="checkbox"/>	<input type="checkbox"/> Eukaryotic cell lines
<input checked="" type="checkbox"/>	<input type="checkbox"/> Palaeontology
<input type="checkbox"/>	<input checked="" type="checkbox"/> Animals and other organisms
<input checked="" type="checkbox"/>	<input type="checkbox"/> Human research participants
<input checked="" type="checkbox"/>	<input type="checkbox"/> Clinical data

Methods

n/a	Involved in the study
<input checked="" type="checkbox"/>	<input type="checkbox"/> ChIP-seq
<input type="checkbox"/>	<input checked="" type="checkbox"/> Flow cytometry
<input checked="" type="checkbox"/>	<input type="checkbox"/> MRI-based neuroimaging

Animals and other organisms

Policy information about [studies involving animals; ARRIVE guidelines](#) recommended for reporting animal research

Laboratory animals

Zebrafish (*Danio rerio*) of Ekkwill, Ekkwill/AB and AB strains were used for this study. Females and males were pooled together. Fish between 3 and 18 months old were used for experiments. To assess regenerating scales in *hsp70l:dnfgfr1-EGFP; osx:ErkKTR-mCherry*; *osx:H2A-mCherry* animals, ~9 weeks old fish were used. To assess developing scales in juvenile fish, fish at the squamation stage were used (~4 weeks old). Transgenic lines used in this study were: *Tg(osx:H2A-mCherry) pd310* (Cox et al.,

2018, Curr Biol); Tg(hsp70l:dnrgfr1-EGFP)pd1 (Lee et al., 2005, Development); Tg(osx:EGFP-CAAX)pd51 (Nachtrab et al., 2013, Development); Tg(osx:mCherry-zCdt1)pd270 (Cox et al., 2018; Curr Bio), Tg(osx:Venus-hGeminin)pd271 (Cox et al., 2018, Curr Bio); Tg(osx:ErkKTR-mCerulean) pd2001 (this study); Tg(osx:H2A-mEos2)pd2002 (this study); Tg(hsp70l:mCherry-2a-fgf20a) (Shibata et al., 2016, Development); Tg(hsp70l:fgf3)x27 (Sweet et al., 2011, Dev Biol).

Wild animals

This study did not involve wild animals.

Field-collected samples

This study did not involve samples collected from the field.

Ethics oversight

All animal experiments were approved by the Institutional Animal Care and Use Committee at Duke University and followed all the relevant guidelines and regulations.

Note that full information on the approval of the study protocol must also be provided in the manuscript.

Flow Cytometry

Plots

Confirm that:

- The axis labels state the marker and fluorochrome used (e.g. CD4-FITC).
- The axis scales are clearly visible. Include numbers along axes only for bottom left plot of group (a 'group' is an analysis of identical markers).
- All plots are contour plots with outliers or pseudocolor plots.
- A numerical value for number of cells or percentage (with statistics) is provided.

Methodology

Sample preparation

Scale regeneration was induced by plucking about 50 scales, in three rows, from each side of osx:H2A-mCherry osx:Venus-hGeminin fish. At 4 days post plucking, all regenerating scales were plucked and collected in PBS on ice. About 3-5 fish were used per sample. Tissue was pelleted by centrifugation (5 min at 600 g) and resuspended in 600 µl of 13 U/ml Liberase (DH-Research Grade - Sigma #5401054001) in HBSS (Gibco #14025-092) and incubated at 37 °C for 1 h. Every 15 min, 500 µl of supernatant was removed, quenched with 65 µl sheep serum (Sigma S2263) on ice, and 500 µl of fresh Liberase was added to the primary tube. All collected supernatant was filtered using 50 µm filters (Corning #431750), pelleted (5 min at 600 g) and resuspended in 1 ml DMEM + 1% BSA (UltraPure - Invitrogen AM2616). Before sorting, 1 µg/ml DAPI (Sigma D9542) was added to the tube.

Instrument

Cells were analyzed and sorted using a SH800S Sony Cell Sorter using a 100 µm disposable chip.

Software

The SH800S Sony Cell Sorter software was used for sorting.

Cell population abundance

Population sizes for flow-cytometry sorted osteoblasts (H2A-mCherry+): Venus-hGeminin- Erk+ cells (9. 10^4, 8. 10^4, 5. 10^4 cells in the three samples); Venus-hGeminin+ Erk- cells (4. 10^4, 5. 10^4, 2. 10^4 cells in the three samples).

Gating strategy

Initially, events were gated using Forward versus Side Scatter Areas (488 nm laser). Then, single cells were enriched by gating Forward Scatter Height versus Forward Scatter Area (488 nm excitation laser). Live cells were enriched by selecting a population with low DAPI emission (405 nm excitation laser). Finally, H2A-mCherry+ Venus-hGeminin- (D in Extended Data Fig. 5e) and H2A-mCherry+ Venus-hGeminin+ (E in Extended Data Fig. 5e) were sorted by gating Venus-hGeminin (488 nm excitation laser) versus mCherry (561 nm excitation laser). Cells were collected in PBS or TriReagent (Sigma T9424).

Tick this box to confirm that a figure exemplifying the gating strategy is provided in the Supplementary Information.